Development of Machines and Process for Laser Additive Manufacturing

M.Tech. Thesis

By
VIVEK RANJAN SINGH

DEPARTMENT OF MECHANICAL ENGINEERING
INDIAN INSTITUTE OF TECHNOLOGY INDORE

MAY 2025

Development of Machines and Process for Laser Additive Manufacturing

A THESIS

Submitted in partial fulfilment of the
requirements for the award of the degree
of
Master of Technology

by
VIVEK RANJAN SINGH

DEPARTMENT OF MECHANICAL ENGINEERING
INDIAN INSTITUTE OF TECHNOLOGY INDORE
MAY 2025

INDIAN INSTITUTE OF TECHNOLOGY INDORE

CANDIDATE'S DECLARATION

I hereby certify that the work which is being presented in the thesis entitled **Development of machines and process for Laser Additive Manufacturing** in the partial fulfilment of the requirements for the award of the degree of **MASTER OF TECHNOLOGY** and submitted in the **DEPARTMENT OF MECHANICAL ENGINEERING, Indian Institute of Technology Indore**, is an authentic record of my own work carried out during the time period from July 2023 to May 2025 under the supervision of Dr. Yuvraj Kumar Madhukar, Associate Professor, Department of Mechanical Engineering, Indian Institute of Technology Indore and Dr. Christ Prakash Paul, Scientific Officer – H, Raja Ramanna Centre for Advance Technology Indore.

The matter presented in this thesis has not been submitted by me for the award of any other degree of this or any other institute.

Vivek Ranjan Singh

This is to certify that the above statement made by the candidate is correct to the best of our knowledge.

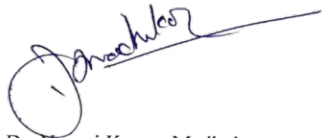

Dr. Yuvraj Kumar Madhukar

Signature of the Supervisor of M.Tech. thesis #1 30/05/2025

Dr. Yuvraj Kumar Madhukar

Signature of the Supervisor of M.Tech. thesis #2 30/05/2025

Dr. Christ Prakash Paul

Vivek Ranjan Singh has successfully given his M.Tech. Oral Examination held on **09/05/2025**.

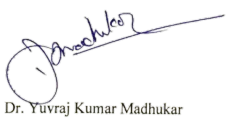

Dr. Yuvraj Kumar Madhukar

Signature(s) of Supervisor(s) of M.Tech. thesis

Date 30/05/2025

Convener, DPGC

Date 02/06/2025

ACKNOWLEDGEMENTS

First and foremost, I would like to express my sincere gratitude to my supervisor, **Dr. Yuvraj Kumar Madhukar**, Associate Professor, Department of Mechanical Engineering, IIT Indore, for his invaluable guidance, continuous support, and encouragement throughout the course of my M.Tech thesis. His dedication to research, insightful feedback, and commitment to scientific rigor have been a constant source of inspiration. Under his mentorship, I have gained valuable technical and academic experience, for which I shall remain deeply grateful.

I would also like to thank **Dr. I. A. Palani**, Course Coordinator for the M.Tech program in Applied Optics and Laser Technology, as well as the faculty and staff of the Department of Mechanical Engineering, IIT Indore, for their support and for providing a stimulating research environment. I extend my sincere thanks to the **Director, Dean of Academic Affairs, Dean of Research and Development, and Dean of Student Affairs**, IIT Indore, for facilitating this academic journey.

I sincerely acknowledge my lab mates at the Laser Material Processing Laboratory, including Mr. Arun Singh, Mr. Shubham Sadhya, Mr. Mukul Jha, Mr. Dipanjan Dey, Dr. Anas Ullah Khan, and Mr. Abneesh Kumar, for their collaborative spirit, constructive discussions, and encouragement throughout various phases of this work.

I am also thankful to my batchmates during the coursework phase Mr. Biswajeet Mishra, Mr. Himanshu Sharma, Mr. Prabhat Dhurve, Mr. Rushikesh Mali, Mr. Shubhi Tiwari, Mr. Shruti Sharma, Mr. Bittu Kumar, and Mr. Naveen Kumar—for their friendship and support.

I am deeply grateful to my project supervisor, **Dr. C. P. Paul**, Scientific Officer-H, RRCAT Indore, for his expert mentorship and scientific guidance throughout the course of this research. His vision, attention to detail, and practical insights were instrumental in shaping the direction of this work. I would also like to express my appreciation to the members of the Engineering Design and Manufacturing Division at RRCAT, particularly Dr. A K Rai, Mr. C. H. Premsingh, Mr. Suresh, Mr. Lalit, Mr. Sokhen Tudu, Mr. C. S. Mandloi, Mr. Anil Adbol, Mr. Ajay, Mr. Neeraj and other members for their assistance in setting up experiments, fine-tuning the laser DED process, and their generous technical support.

I extend my thanks to Mr. Saurav Kumar Nayak, Mr. Sunil Yadav, Ms. Kirthika, and other Ph.D. scholars at RRCAT for their support, discussions, and assistance throughout the project.

I am also thankful to the team at the AIC-Pi HUB Foundation, whose industry-oriented insights and infrastructure support significantly contributed to the experimental execution of this research. I would especially like to thank Mr. Shriyansh Bhagwat, Mr. Lalit Bajaj, and Mr. Rahul for their engagement and collaboration during key phases of the project.

On a personal note, I am eternally grateful to my parents and family for their unconditional love, moral support, and belief in me. I would like to acknowledge the immense encouragement I received from my parents, **Mr. Aditya Kumar Singh and Mrs. Saroj Singh**, whose unwavering faith in me helped me overcome every challenge. I am also deeply thankful to my elder brother, **Mr. Abhishek Ranjan Singh**, for his constant motivation and support throughout this academic journey.

- ***Vivek Ranjan Singh***

Indian Institute of Technology Indore

DEDICATION

I dedicate this thesis to my beloved family—my mother, Mrs. Saroj, my father, Mr. Aditya Kumar Singh, and my brother, Mr. Abhishek Ranjan Singh—for their unwavering love, support, and belief in me.

To my brother, whose determination and achievements have always inspired me, thank you for being a constant source of motivation throughout my journey.

ABSTRACT

Laser Directed Energy Deposition (L-DED) has emerged as a powerful additive manufacturing technique for high-performance alloys, owing to its ability to fabricate complex, near-net-shape components. However, achieving consistent geometric accuracy remains a major challenge, especially for multi-layer thin-walled structures of high-performance alloys like In718. This thesis presents a comprehensive, experimentally validated, data-driven framework for predicting and optimising geometric features—track height, width, and depth—in L-DED. A systematic experimental study was conducted using a structured design approach to understand how laser power, scan speed, and powder feed rate affect the geometry of L-DED deposits. By analysing the resulting data, clear trends emerged: laser power and powder feed rate were found to be the dominant factors influencing Track width and height, while scan speed played a more subtle role in melt pool behaviour and stability. These trends were used to develop predictive relationships that guided process optimisation. The optimised parameters enabled significant improvements in material efficiency, energy consumption, and build accuracy. Building on this, the study was extended to multi-layer thin-wall structures, where the introduction of interlayer time delay served as a key thermal control strategy. A 4-second delay was identified as optimal, resulting in enhanced mechanical performance with an ultimate tensile strength of approximately 1002 MPa and ductility of around 37.5%, highlighting the importance of managing thermal history during deposition.

To demonstrate real-world applicability, a 3D thin-walled mesh structure of 42 mm × 42 mm with 10 mm height was successfully fabricated using the optimized parameters. This final build validated the model's predictive strength and scalability. The framework provides a solid foundation for future integration with in-situ thermal monitoring to enable intelligent, adaptive control in additive manufacturing.

LIST OF PUBLICATIONS

In refereed conference

1. 32nd DAE BRNS National Laser Symposium: **Vivek Ranjan Singh**, A. Kumar, N. Pandey, and I. A. Palani, “Investigating laser surface strategy to develop hydrophobic aluminium surface using microsecond pulsed Yb doped fiber laser," in Proc. 32nd DAE BRNS Nat. Laser Symp. (NLS-32), Indore, India, 2024, pp. 548–551. Available: https://www.ila.org.in/nls32
2. 13th International Conference on Precision, Meso, Micro and Nano Engineering: S. Sadhya, **Vivek Ranjan Singh**, A. Kumar, S. Chatterjee, and Y. K. Madhukar, “Dependency of Wire Feed Direction in TIG-Based Wire Arc Additive Manufacturing” presented at the 13th Int. Conf. on Precision, Meso, Micro, and Nano Engineering (COPEN 13), Kozhikode, India, Dec. 13–15, 2024.

TABLE OF CONTENTS

LIST OF FIGURES

LIST OF TABLES

NOMENCLATURE

AS	Surface area of indentation (mm^2).
d_1, d_2	Diagonals of indentation (mm).
d_{avg}	Average diagonal length (mm).
F	Applied load in vickers test (kgf).
HV	Vickers hardness number.
O1	Track width (mm).
O2	Track height (mm).
O3	Track depth (mm).
P1	Laser power (watts).
P1W	Laser power (watts).
P2	Scan speed (mm/min).
P2S	Scan speed (mm/min).
P3	Powder feed rate (g/min).
P3G	Powder feed rate (g/min).
TD	Interlayer time delay (sec.).
TVASHTR	Name of the indigenous DED machine system used.
UTS	Ultimate Tensile Strength (Mpa).
W/H	Aspect ratio of track.

ACRONYMS

AM	Additive manufacturing.
ANOVA	Analysis of variance.
ASTM	American Society for Testing and Materials.
CAD	Computer-aided design.
DED	Direct energy deposition.
DfAM	Design for additive manufacturing.
DLP	Digital light processing.
DOE	Design of experiment.
EDM	Electro discharge machining.
EDS	Energy dispersive x-ray spectroscopy.
FDM	Fused deposition modelling.
KNN	K-nearest neighbours.
LCD	Liquid crystal display.
L-DED	Laser direct energy deposition.
LOM	Laminated object manufacturing.
PBF	Powder bed fusion.
RRCAT	Raja Ramanna Centre for Advanced Technology.
RSM	Response surface methodology.
SEM	Scanning electron microscopy.
SLA	Stereolithography.
SLM	Selective laser melting.
SVM	Support vector machine.
UAM	Ultrasonic additive manufacturing.
UTM	Universal testing machine.

Chapter 1

Introduction, Literature Review & Objective

Additive Manufacturing (AM), often referred to as 3D printing, represents a transformative approach to fabrication, fundamentally distinct from traditional subtractive or formative techniques. It is defined as a process of creating objects by sequentially adding material, typically layer by layer, based on digital 3D models [1]. This innovative manufacturing paradigm offers unparalleled freedom in design, material utilization, and production flexibility [2].

As a groundbreaking technology enabling the fabrication of complex geometries that are often unattainable through traditional manufacturing routes, AM builds components layer by layer, precisely depositing material only where required [3]. Unlike subtractive processes which remove material from a larger block, this approach allows for enhanced material utilization, reduced waste, and design freedom that enables the creation of intricate internal structures and lightweight parts [4].

1.1 Classification of Additive Manufacturing

According to ISO/ASTM 52900:2001, Additive Manufacturing processes are classified into seven primary categories based on the type of feedstock and energy source employed during fabrication:

1.1.1 Vat Photopolymerization

Vat Photopolymerization is one of the earliest and most precise additive manufacturing techniques, wherein a liquid photopolymer resin is selectively cured using a light source. The process takes place in a vat filled with photoreactive resin, where the build platform descends layer by layer as the resin is selectively solidified based on sliced CAD data. Curing is achieved using either a laser, projector, or backlit panel depending on the subtype of the process. This technique is particularly renowned for its high resolution, excellent surface finish, and suitability for detailed prototypes, dental models, and microfluidic structures. The key limitation lies in the brittleness of cured photopolymer resins and the need for post-curing and support removal.

A. **Stereolithography (SLA)** It uses a focused ultraviolet (UV) laser to trace and cure each cross-section of the model on the surface of the liquid resin. After each layer is cured, the platform lowers slightly, allowing a fresh layer of resin to coat the part, and the process repeats.

B. **Digital Light Processing (DLP)** employs a digital light projector to flash an entire layer image at once, solidifying an entire cross-section simultaneously rather than point-by-point.

C. **Liquid Crystal Display (LCD)** Printing shares similarities with DLP but uses an array of UV LEDs beneath an LCD panel to mask and expose selected regions of resin in each layer.

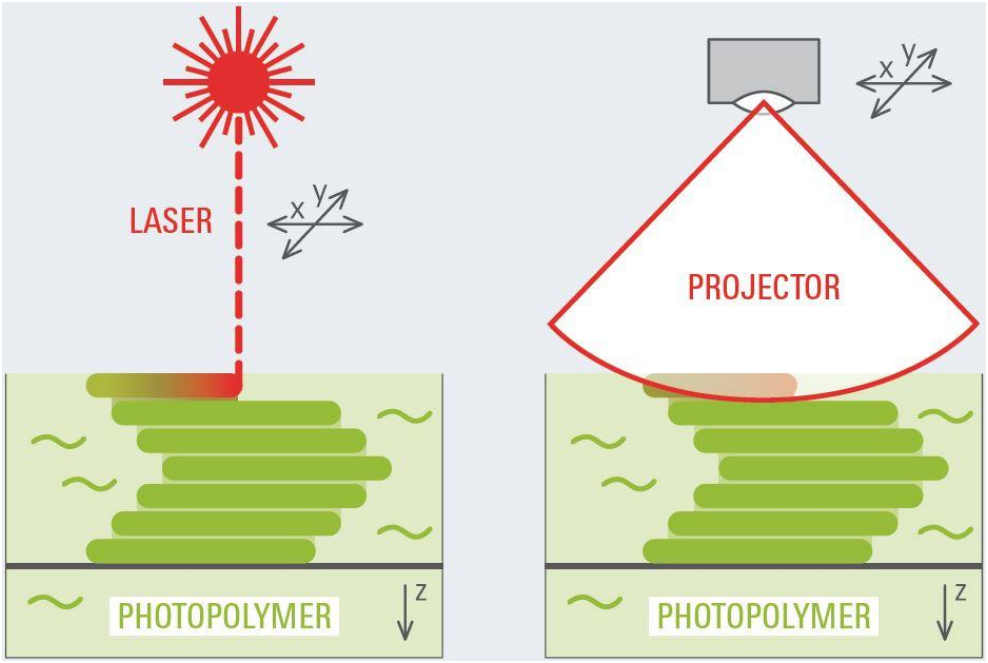

Fig. 1.1: Illustration of VAT polymerisation (a) SLA (b) DLP [5].

1.1.2 Material Jetting

Material Jetting is an additive manufacturing technique wherein droplets of build material are selectively deposited onto a substrate to form a part layer by layer. Similar in principle to inkjet printing, this process allows for precise material placement and excellent surface finish. A key advantage of material jetting is its ability to process multiple materials within a single build, including combinations of rigid, flexible, and support materials. This makes it particularly suitable for prototyping complex assemblies, functional parts with embedded

features, and full-color models. The printed part is typically cured by UV light or thermal energy immediately after deposition to ensure dimensional stability.

A. **Drop-on-Demand (DOD) jetting** involves the deposition of discrete droplets of material only where needed, guided by CAD-based slicing instructions. Each droplet is deposited via thermal or piezoelectric actuation.
B. **Multi-Material Jetting** builds upon the principles of DOD but enables the simultaneous deposition of multiple build materials in a single layer.
C. **Wax Jetting,** a specialized variant, utilizes wax-like materials that are jetted and then solidified layer by layer.

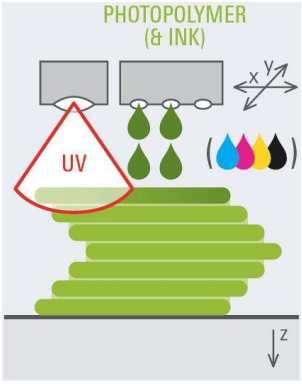

Fig. 1.2: Illustration of Material Jetting process [6].

1.1.3 Binder Jetting

Binder Jetting is an additive manufacturing process in which a liquid binder is selectively deposited onto a powder bed to join powder particles and build a part layer by layer. Unlike processes that involve melting or sintering during deposition, Binder Jetting forms a "green part" that typically requires post-processing—such as sintering, infiltration, or curing—to achieve final strength and density.

A. **Metal Binder Jetting** is commonly used for producing metal components in their green state, which are later sintered in a furnace to attain the desired mechanical and metallurgical properties. This approach avoids the high thermal input and residual stresses associated with laser-based metal printing.

B. **Sand Binder Jetting** is widely used in the foundry industry for creating sand molds and cores used in metal casting. In this process, a binder selectively joins layers of sand particles to form the desired mold shape, eliminating the need for tooling and allowing for the rapid production of complex geometries.

C. **Ceramic Binder Jetting** applies the same principles to ceramic powders.

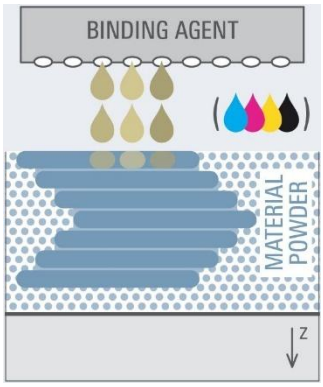

Fig. 1.3: Illustration of Binder Jetting [7].

1.1.4 Material Extrusion

Material extrusion is one of the most accessible and widely utilized categories of additive manufacturing. In this process, material is selectively dispensed through a nozzle by mechanical or pneumatic force to build parts layer by layer according to a digital model. Typically, the material is heated to a semi-molten state as it is extruded and then solidifies upon deposition.

A. **Fused Deposition Modeling (FDM),** also referred to as Fused Filament Fabrication (FFF), is the most commonly recognized form of material extrusion. It uses a spool of thermoplastic filament, such as PLA, ABS, or polycarbonate, which is fed through a heated nozzle. As the filament melts, it is deposited in successive layers on the build platform

B. **Pellet Extrusion** is a variant of FDM that uses raw thermoplastic pellets instead of filament. This method allows for faster material deposition rates and reduces material cost, making it suitable for large-scale applications.

C. **Concrete Extrusion**, a cement-based mixture is extruded through a nozzle in successive layers to build structural components such as walls, housing units, and infrastructure elements.

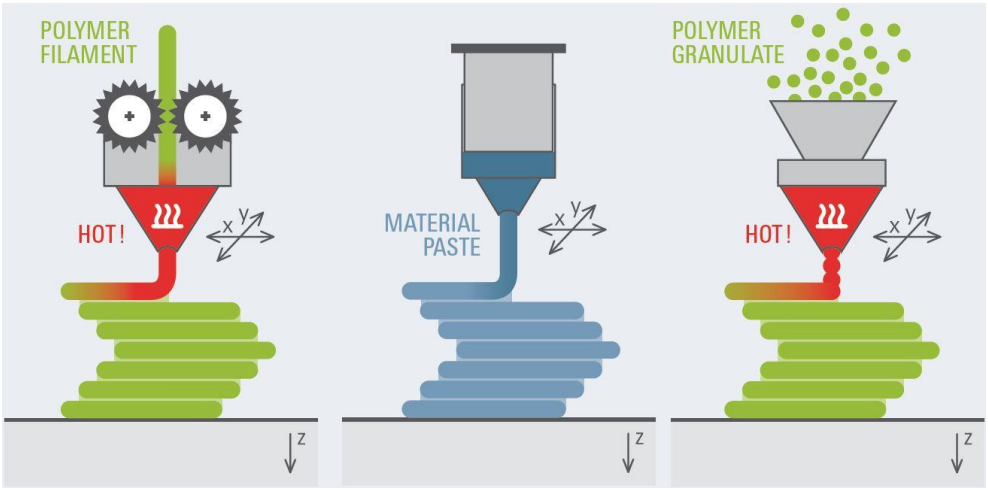

Fig. 1.4: Illustration of Material Extrusion process, (a) FDM (b) Concrete & (c) Pellete [8].

1.1.5 Powder Bed Fusion (PBF)

Powder Bed Fusion (PBF) is one of the most widely adopted additive manufacturing categories for both metallic and polymeric components. In this process, a thin layer of powder is spread over a build platform, and a high-energy thermal source—either a laser or an electron beam—is used to selectively fuse the powder particles based on cross-sectional data from a 3D CAD model. After each layer is fused, the platform is lowered, and a new powder layer is spread for the next cycle. The process repeats layer by layer until the part is complete.

A. **Selective Laser Sintering (SLS)** is primarily used for polymer powders, such as nylon (PA12), TPU, or composite-filled variants. A CO_2 laser selectively sinters the powder without fully melting it, resulting in parts with good strength and thermal resistance.

B. **Selective Laser Melting (SLM)**, also referred to as Laser Powder Bed Fusion (LPBF), fully melts metal powders such as stainless steel, aluminum, titanium, or Inconel to produce fully dense parts. A high-

power fiber laser traces each layer with extreme precision, allowing for the fabrication of intricate geometries with fine details.

C. **Electron Beam Melting (EBM)** uses an electron beam, rather than a laser, to melt metal powder in a vacuum environment.

D. **Direct Metal Laser Sintering (DMLS)** is closely related to SLM but is optimized for specific metal alloys and is often used with proprietary powder formulations.

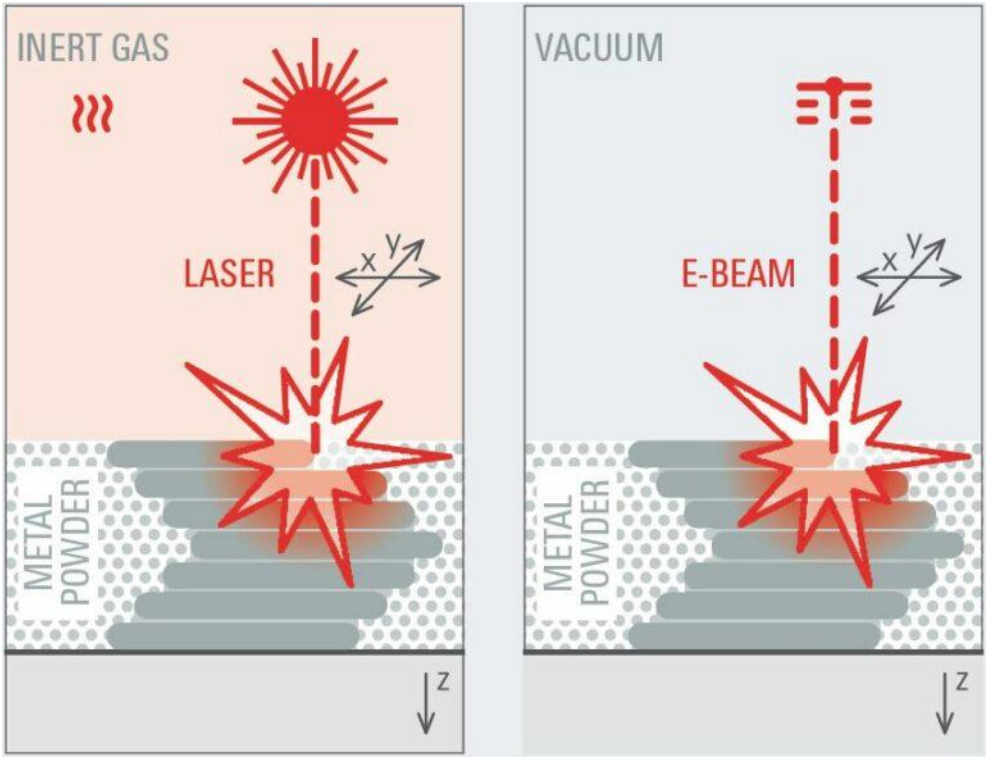

Fig. 1.5: Illustration of Powder Bed Fusion [9].

1.1.6 Directed Energy Deposition (DED)

Directed Energy Deposition (DED) is an advanced additive manufacturing process wherein material is deposited and simultaneously melted using a focused thermal energy source. Unlike powder bed fusion systems, DED systems typically use a nozzle mounted on a multi-axis arm or gantry to deposit material directly onto the build surface, enabling the fabrication of large, complex components or the repair of existing parts. Feedstock can be in the form of powder or wire, and the process is capable of handling a wide range of metals and alloys. The high deposition rates and ability to deposit material onto non-planar surfaces make DED highly suitable for industrial applications such

as aerospace repair, tooling, and hybrid manufacturing. However, due to its open-path nature, DED may offer lower resolution and surface finish compared to powder bed methods, necessitating post-processing.

A. **Laser-Based DED** (DED-LB) is the most commonly adopted form of DED and utilizes a high-power laser beam as the energy source.
B. **Electron Beam DED** (DED-EB) employs an electron beam under vacuum conditions to provide the thermal energy necessary for melting the feedstock.
C. **Plasma Arc DED** uses a plasma arc as the heat source to melt the feed material, usually wire, during deposition.

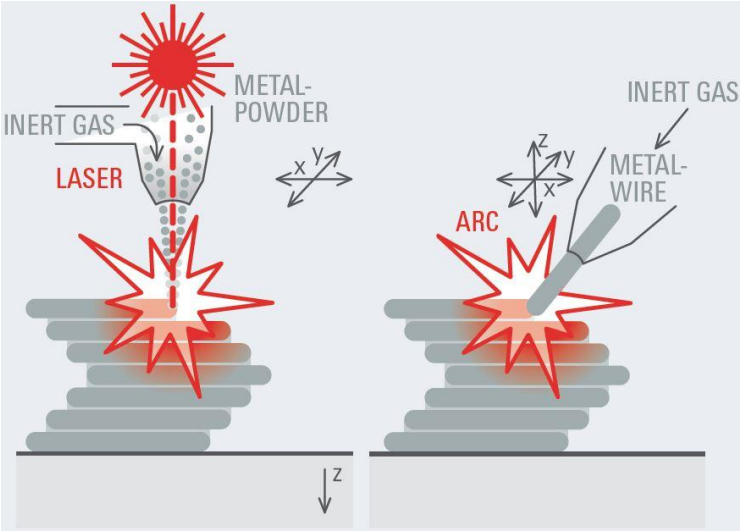

Fig. 1.6: Illustration of Direct Energy Deposition [10].

1.1.7 Sheet Lamination

Sheet Lamination is a category of additive manufacturing where successive sheets of material are bonded together to form a three-dimensional object. Unlike extrusion or powder-based techniques, this method utilizes prefabricated sheets—typically paper, plastic, or metal—which are cut to shape and stacked in layers. The bonding process can be achieved through adhesives, heat, or ultrasonic energy, depending on the specific technology employed.

A. **Laminated Object Manufacturing** (LOM) is one of the earliest forms of sheet lamination. In this process, adhesive-coated sheets (usually

paper or plastic) are unwound onto a build platform and bonded layer-by-layer using a heated roller.

B. **Ultrasonic Additive Manufacturing (UAM)** is a more advanced form of sheet lamination used primarily for metal components. It employs ultrasonic vibrations combined with pressure to weld thin metal foils together in a solid-state process, avoiding the melting typically seen in other AM methods.

Each classification addresses different material types, build strategies, and application domains, allowing engineers to select the most appropriate technique based on performance, geometry, and economic constraints.

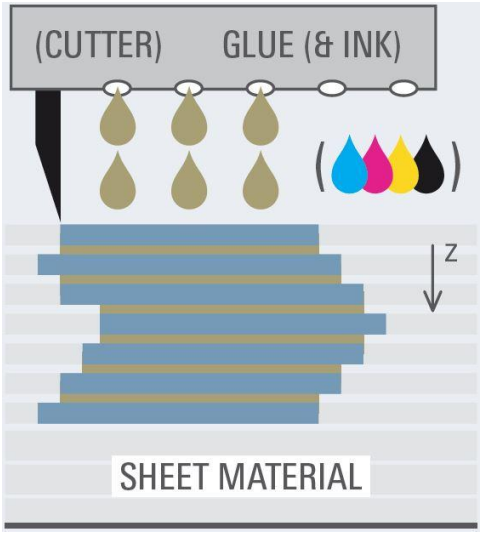

Fig. 1.7: Illustration of Sheet Lamination [11].

1.2 Design for Additive Manufacturing

Design for Additive Manufacturing (DfAM) is a specialized design approach that goes beyond conventional CAD modelling [12]. While the basic process of additive manufacturing begins with the creation of a 3D digital model—typically using CAD software—which is then converted into a Standard Tessellation Language (STL) file, the implications for DfAM extend far deeper into how parts are conceived, optimized, and produced [13].

The STL file, once generated, is sliced into discrete layers, each representing a cross-section of the part. These layers are then translated into machine-readable

tool paths and commands which guide the 3D printer during fabrication [14]. While this workflow represents the standard pipeline for any AM process, designing for AM involves deliberately tailoring the part geometry and process strategy to enhance performance, reliability, and manufacturability [15].

DfAM focuses on several critical objectives:

A. **Minimization of Manufacturing Defects:** Strategies are employed to reduce the likelihood of issues such as porosity, lack of fusion, and thermal distortion. This includes the optimization of scanning paths, support structure design, and thermal simulation [16].
B. **Enhancement of Mechanical Properties:** Through controlled grain orientation, layer bonding, and parameter tuning, the final mechanical properties of additively manufactured parts can be made comparable or even superior to those produced by traditional means [17].
C. **Cost-Effectiveness and Resource Optimization:** A key challenge in AM is balancing performance with process economy. Efficient designs aim to reduce build time, material usage, and post-processing requirements, thus improving overall feasibility for industrial applications.
D. **Facilitating Future Applications:** DfAM plays a pivotal role in paving the way for new engineering applications by enabling the creation of parts that are lighter, stronger, and functionally integrated. With advancements in simulation and topology optimization, DfAM is becoming increasingly data-driven and predictive.

1.3 Literature Overview

Additive manufacturing (AM) of Ni-based superalloys like Inconel 718 is of growing interest for high-performance applications in aerospace, energy, and automotive sectors due to the alloy's exceptional high-temperature strength, corrosion resistance, and weldability [18], [19]. Inconel 718 (IN718) has become one of the most studied materials for laser-based additive processes such as Laser Powder Bed Fusion (L-PBF) and Laser-Directed Energy Deposition (L-DED) [20], [21]. While significant work has been carried out on

understanding the process-structure-property relationships in AM IN718, challenges persist in achieving high geometric fidelity, optimizing process parameters, and developing predictive models for as-built component geometry. This section provides a structured review of the literature across four thematic areas

- Mechanical and microstructural characteristics of AM IN718
- Modeling approaches (thermal, analytical, statistical, and data-driven)
- Deposition strategy and process parameter effects
- Geometrical predictability and gaps in multilayer structure modeling

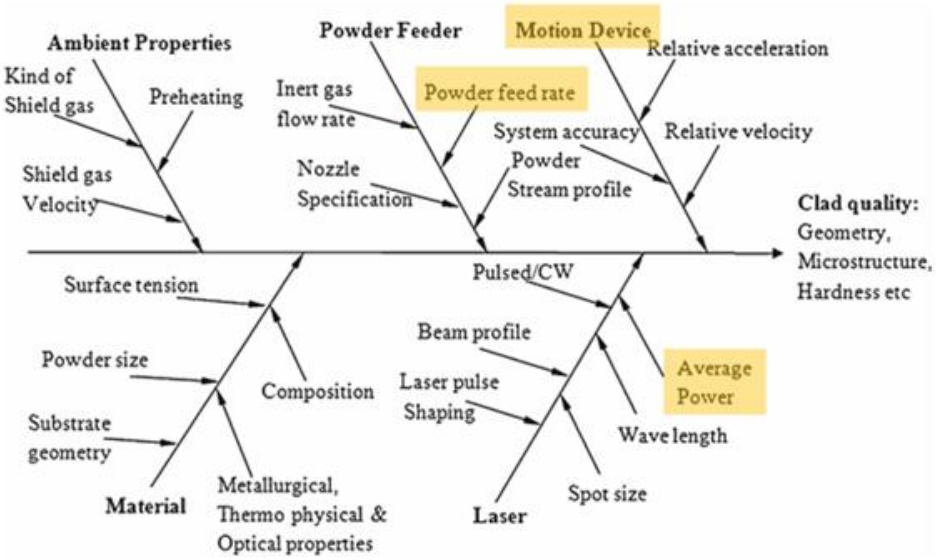

Fig. 1.8: Fish diagram showing factors affecting laser powder DED [22].

1.3.1 Additive Manufactured Inconel 718

IN718, a nickel-based superalloy, is a widely used material in additive manufacturing due to its high-temperature strength and corrosion resistance. However, its performance is sensitive to microstructural evolution during deposition.

A. Mechanical Properties

Laser-AM Inconel 718 generally achieves tensile strengths comparable to or exceeding those of wrought/cast material [18], [23], [24]. Zhang et al. reported that room- and high-temperature

properties of SLM-fabricated IN718 are “equivalent to or even higher than” wrought counterparts [25]. Kurdi et al. measured hardness values between 330–349 HV for PBF-IN718, which is slightly lower than the ~408 HV seen in cast versions due to the absence of γ′/γ″ precipitates in the as-built condition [19]. These strength levels indicate that without post-build aging, the metastable AM microstructure sacrifices some strength but remains mechanically viable.

Fatigue behavior in AM 718 has also drawn interest, although fatigue life is often limited by porosity, anisotropy, and lack-of-fusion defects [26]. Nonetheless, studies such as Hosseini et al. [18] suggest that with adequate heat treatment and optimized process settings, fatigue life can approach that of wrought material.

B. Microstructural Characteristics

AM IN718 typically develops a cellular-dendritic structure due to rapid cooling and solidification under laser melting [19], [23], [27], [28]. Kurdi et al. observed that PBF-IN718 contains long columnar grains growing epitaxially along the build direction, with interlocking sub-cell structures at the nanoscale [19]. These structures also promote Nb and Ti segregation in the interdimeric regions, resulting in Laves phase formation [29]. These brittle intermetallic phases may degrade ductility and cause crack initiation under load. Heat treatment dissolves Laves and promotes γ′ and γ″ precipitation, improving strength [23], [30] .

The presence of δ-phase at grain boundaries in as-built samples has also been reported, and controlling its morphology and distribution is crucial for ensuring optimal creep resistance [24], [31]. Thus, both thermal history and post-processing are pivotal in tailoring the mechanical performance of AM IN718

1.3.2 Modelling Techniques

Additive Manufacturing (AM), particularly Laser-based Directed Energy Deposition (L-DED), has been extensively studied using a variety of modelling

techniques. These can broadly be categorized into thermal, analytical, and statistical models.

A. Thermal Models

Thermal models are often physics-based and rely on finite-element or computational fluid dynamics simulations to predict temperature fields, melt pool behaviour, and cooling rates. For example, Fang et al. developed a 3D finite-element thermal model for multi-layer IN718 builds and validated it against infrared thermography, showing how thermal histories could be used to predict mechanical properties through machine learning [32], [33]. Similarly, Shin et al. used coupled thermal-fluid models to simulate the geometry evolution in DED tracks and found strong agreement between simulated and experimental track shapes [34].

B. Analytical Model

Analytical models, although less computationally intensive, provide closed-form solutions for simpler cases. They often use the Rosenthal moving heat source theory or empirically derived formulas to relate process parameters to melt pool dimensions. While efficient, these models are less accurate for predicting complex geometries or multi-layer builds due to simplifications like constant thermal properties or neglect of fluid flow [35].

C. Statistical models

Statistical models offer a data-driven alternative by directly correlating input process parameters—such as laser power, scan speed, and powder feed rate—with output geometries like track width, height, and dilution. Approaches like Taguchi design and Response Surface Methodology (RSM) have been widely applied for parameter optimization in L-DED of IN718 [36], [37], [38], [39], [40], [31]. Biyikli et al. [41] demonstrated that bead height and wetting angle in single-track IN718 deposits could be predicted using power-law regression models derived from experimental data, showing strong alignment between modeled and experimental results. Xv et al. [27] implemented a combination of ML and regression analysis to model and optimize clad geometry, achieving high R^2 values and confirming the predictive robustness of

statistical modeling. Ribeiro et al. [37] extended this methodology by applying RSM to identify optimal parameter combinations for clad thickness and width, followed by experimental validation.

Building on this foundation, Ravichander et al. [24] and Xv et al. [27] employed advanced machine learning (ML) techniques—including artificial neural networks (ANN) and ensemble models—to predict bead geometry and mechanical properties in IN718 laser cladding. These models demonstrated high predictive fidelity across multiple outputs, including height and microhardness, particularly in multi-parametric scenarios.

Despite extensive exploration of individual modeling strategies—be it thermal, analytical, or statistical—very few studies have successfully integrated statistical or machine learning models with full experimental validation, particularly for geometry prediction in multi-layer thin-walled structures. This lack of holistic integration highlights a significant research opportunity to develop predictive frameworks that are not only accurate but also generalizable to real-world additive manufacturing applications. Addressing this gap is especially critical for advancing Design for Additive Manufacturing (DfAM), where achieving precise geometric accuracy is essential to minimize post-processing and ensure functional performance.

1.3.3 Deposition Strategy and Parameter Effects

The final part geometry in L-DED is heavily influenced by process parameters. Laser power, scan speed, and powder feed rate each affect the melt pool dynamics and deposition volume [42].

Higher laser power generally increases track width and depth by enlarging the melt pool. Conversely, faster scan speeds reduce energy input per unit length, resulting in thinner and narrower beads. Biyikli et al. observed that track height increased with power and feed rate, while scan speed had an inverse effect [41]. Xv et al. found that laser power was the most dominant factor influencing width, while scan speed played a greater role in height and penetration depth [27].

Powder feed rate adds complexity—too low, and the bead may be discontinuous; too high, and incomplete melting may occur. It is showed that optimal feed rates improved bead consistency, but also highlighted the risk of excessive build-up and porosity at high deposition rates [26], [43].

Moreover, deposition strategies like layer overlap, scanning pattern, and inter-layer dwell time affect heat accumulation and residual stress. Advanced scan strategies have been proposed to mitigate heat build-up, but most rely on real-time feedback or closed-loop systems, which are not yet standard practice [35].

Process parameters—including laser power, scan speed, powder feed rate, and layer thickness—significantly influence geometry, microstructure, and defects in AM IN718 [41], [44], [45].

A. **Laser Power**: Increased power generally yields wider and deeper melt pools but may cause keyholing if excessive [35].
B. **Scan Speed**: Faster scan speeds reduce energy density, increasing the likelihood of lack-of-fusion porosity [26].
C. **Powder Feed Rate** (in DED): High feed rates can increase bead height but lead to porosity and poor bonding if not matched with sufficient energy input [37].
D. **Layer Thickness and Hatch Spacing**: Finer layers and tighter hatch spacing promote densification but increase build time and residual stresses [46].

Ribeiro et al. analyzed how each of these factors affects the geometry of single-pass laser cladding in IN718 and presented empirical models to predict height and width [37]. Kumar et al. explored porosity dependence on scan speed and power, optimizing L-PBF IN718 for density exceeding 99% [26].

Deposition strategies such as zig-zag scanning and interlayer rotation are employed to minimize thermal gradients and residual stress buildup [47].

While prior work has quantified parameter influence on single-layer or simple geometries, predicting geometry in multi-layer builds remains a challenge. This

motivates the development of predictive models tailored for geometric accuracy.

1.3.4 Geometrical Predictability

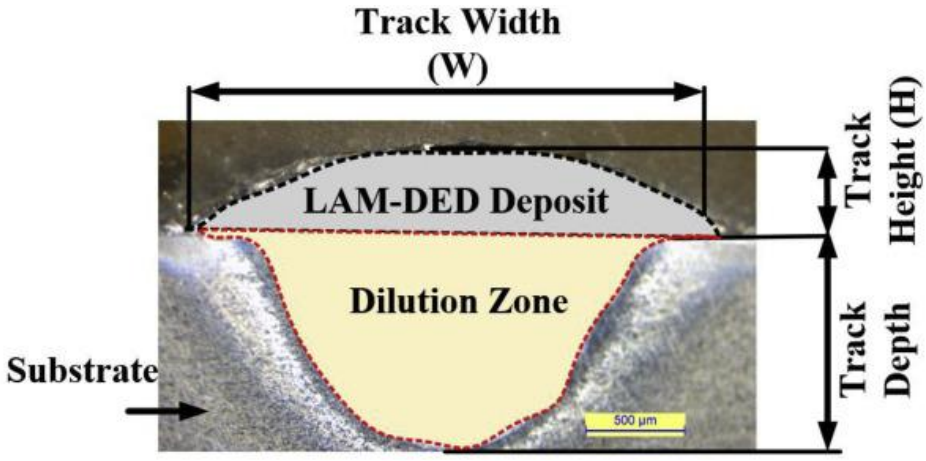

Fig. 1.9: Laser DED track illustration [42].

Several researchers have emphasized that geometrical accuracy is a primary constraint in Design for Additive Manufacturing (DfAM), particularly for components intended to undergo minimal or no post-processing. If a deposited part is dimensionally inaccurate, subsequent enhancements to mechanical properties—such as aging or hot isostatic pressing (HIP)—cannot compensate for the initial geometric deviation. This makes accurate geometry prediction critical to ensuring functionality and reducing post-build intervention.

The challenge is especially pronounced in multi-layer, thin-walled structures, where cumulative errors over successive layers can lead to pronounced defects such as crown formation, edge overbuild, and warping. Despite its importance, literature reveals a significant lack of validated predictive models tailored for these complex geometries.

Geometric prediction remains difficult due to factors like dynamic melt pool behavior, residual stress accumulation, and layer-wise distortion during the build process [48], [29]. Ravichander et al. [24] reported similar success using response surface methodology (RSM) and artificial neural networks (ANN) for predicting clad thickness and microhardness. Xv et al. [27] further advanced this area using ensemble learning models, which outperformed traditional linear regression in multi-output prediction tasks, such as bead height and surface roughness.

However, most of these studies are limited to single-bead or simple wall geometries, with few addressing the complex thermal and mechanical interactions seen in multi-layer, thin-wall structures [49].

Key Findings:

A. Empirical and machine learning models have demonstrated strong accuracy for predicting single-track geometry [24], [27].

B. Very few studies explicitly model distortion, crown effect, or edge overbuild in multi-layer builds [48] .

C. Integrated predictive frameworks that couple thermal, mechanical, and geometrical modeling remain largely underdeveloped.

1.4 Motivation

While numerous studies have modelled AM IN718 using regression and ML, most focus on limited geometries like single-track or small cuboid builds. Comprehensive models that accurately predict geometrical features such as wall thickness, surface waviness, and overall dimensional error in multi-layer LAM IN718 parts are scarce. Existing models also underutilize experimental validation and often lack generalizability. Moreover, most predictive efforts focus on microstructure or mechanical properties, with geometry taking a secondary role despite its importance in minimizing post-processing [18], [48].

1.4.1 Problem Statement

The primary aim of this study is to develop an experimentally validated, data-driven predictive framework for geometrical features in Laser Additive Manufacturing of Inconel 718. By integrating full factorial experimentation with statistical and machine learning models, the goal is to predict and optimize key geometric outcomes such as bead width, height, and wall thickness under varying process conditions.

1.4.2 Objectives of The Study

The primary objective of this study is to optimize the Laser-Directed Energy Deposition (L-DED) process for Inconel 718 by establishing accurate, predictive relationships between input process parameters and resulting track

geometries. To achieve this, the study adopts a data-driven approach combining statistical modelling and experimental validation. The insights gained are intended to improve process control, minimize resource consumption, and support the development of robust Design for Additive Manufacturing (DfAM) strategies that integrate predictive modelling into fabrication planning.

The specific objectives of this work are as follows:

- **A.** To develop and evaluate statistical prediction models that correlate laser power, scan speed, and powder feed rate with deposition geometry (height, width, and depth).
- **B.** To incorporate these models into an optimization framework aimed at reducing build time, material usage, and energy consumption.
- **C.** To experimentally validate the prediction and optimization models using both single-track and multi-layer deposition trials.
- **D.** To demonstrate the practical utility of predictive models in guiding process planning for complex builds.
- **E.** To contribute to the advancement of DfAM methodologies by integrating predictive modelling with real-time fabrication insights.

1.5 Organisation of Thesis

Chapter 1: Introduction**,** Literature review focusing on existing studies in laser-based DED, Process Parameter Influence, predictive modelling efforts and an outline of the research scope.

Chapter 2: Experiment Methodology detailing the selection of process parameters, use of design of experiments (DOE) for efficient trial planning, and strategy for capturing geometric and mechanical trends.

Chapter 3: Experimental Setup and Instrumentation describing the laser DED system, material specifications, measurement techniques, and characterization tools employed in the study

Chapter 4: Objective, Results and Discussion presenting model development, optimization outcomes, multi-layer deposition analysis, and mechanical performance evaluation with critical insights

Chapter 5: Conclusion and Future Scope summarizing the key findings, demonstrating the capability of the developed framework, and proposing future directions for intelligent L-DED processing

Chapter 2

Experiment Methodology

The experimental framework for this study was systematically structured to achieve the dual objectives of process characterization and predictive model development for Laser Additive Manufacturing (LAM) using Inconel 718 powder. The methodology consisted of sequential phases, each building upon the insights gained in the preceding stage to ensure robust model training, validation, and implementation. The entire design was guided by scientific principles of statistical analysis, design of experiments (DOE), and data-driven optimization. The major components of the experimental design are outlined below:

2.1 Preliminary Trial Experimentation and Statistical Analysis

The first stage of the experimental work involved conducting a series of preliminary deposition trials to qualitatively and quantitatively assess the influence of key process parameters—namely laser power, scan speed, and powder feed rate—on track geometry. These initial trials were analyzed using Analysis of Variance (ANOVA) to determine the statistical significance and relative contribution of each input factor on the output responses, such as track height and width. The results of ANOVA informed the selection of parameter ranges and justified the structure for the next phase of controlled experimentation.

2.2 Full Factorial Experimental Matrix

Following the identification of key influential factors, a full factorial experimental design was adopted. This approach enabled the comprehensive exploration of interactions among parameters across multiple levels. A full factorial matrix was constructed involving three independent variables (laser power, scan speed, and powder feed rate), each varied over a defined number of levels.

Table 2.1: Full factorial experiment design.

Level→ Parameter ↴	1	2	3
Powder Feed Rate	4.7	6.0	7.6
Power in Watts	700	800	900
Scan Speed mm/min	400	500	600

This yielded a dataset rich in variability, which is essential for the development of accurate and generalizable predictive models. In total, 27 single-track deposition samples were fabricated under controlled conditions, and their geometric characteristics were measured using optical microscopy.

2.3 Development and Evaluation of Predictive Models

The dataset obtained from the full factorial experiments served as the input for the exploration of various machine learning and statistical modeling approaches. These included Support Vector Machines (SVM), Decision Trees, Random Forests, K-Nearest Neighbors (KNN), and Polynomial Regression. Each model was evaluated based on metrics such as R^2 score, root mean square error (RMSE), and visual correlation between predicted and actual values. Based on comparative performance analysis, a hybrid modeling approach was selected: Polynomial Regression was used for predicting width and height, while Random Forest was chosen for depth prediction due to its superior accuracy and robustness against overfitting.

2.4 Model Validation Through Experimental Depositions

To assess the predictive accuracy of the selected hybrid model, a validation step was carried out. New deposition trials were conducted using parameter combinations not included in the training dataset. The experimental outcomes were then compared with the model predictions to verify accuracy. This step

was critical to confirming the model's applicability in real-world deposition tasks and provided insights into its limitations and boundary conditions.

2.5 Optimization Framework Based on Predictive Model

Upon successful validation, the predictive model was integrated into an optimization framework for process parameter selection. The optimization objective was to minimize deposition time, powder consumption, and energy usage while achieving a target geometry. A custom cost function incorporating build time, material usage, and energy consumption was defined. The model then served as a surrogate function to predict deposition outcomes during iterative optimization, thus eliminating the need for time-consuming physical experiments during process planning.

2.6 Introduction of Multi-Layer Deposition Control

Building on the single-track insights, the experimental methodology was extended to address multi-layer deposition challenges. This included the introduction of additional control parameters such as inter-layer delay time and overlap strategy. These variables were identified as crucial for maintaining structural integrity, preventing heat accumulation, and ensuring dimensional accuracy in multi-layered builds.

2.7 Final Thin-Wall Deposition and Demonstration

The final stage involved the fabrication of a thin-walled multi-layer geometry using the optimized process parameters. This demonstration served as a proof-of-concept for the developed prediction and optimization framework. The fabricated component was subjected to geometrical and mechanical evaluations to assess build quality, thereby concluding the experimental validation of the entire research approach.

Chapter 3

Experimental Setup and Instrumentation

The experimental investigations were conducted using the TVASHTR Laser DED system, an indigenously developed platform by the Laser Additive Manufacturing Laboratory, part of the Engineering Design and Manufacturing Division at Raja Ramanna Centre for Advance Technology, Indore. This setup is tailored for precision deposition of metallic powders using laser-based directed energy deposition (DED) techniques and incorporates a variety of subsystems enabling controlled multi-axis additive manufacturing.

Fig 3.1: TVASHTR LAM DED system.

3.1 Machine Setup

The system comprises a vacuum-sealable glove-box-style chamber, allowing optional inert or controlled atmosphere processing. The deposition head features a coaxial powder-feed nozzle, which is integrated into a three-axis gantry system. The build platform is further enhanced with two additional axes of rotation, facilitating five-axis deposition strategies for complex geometries and curved surfaces.

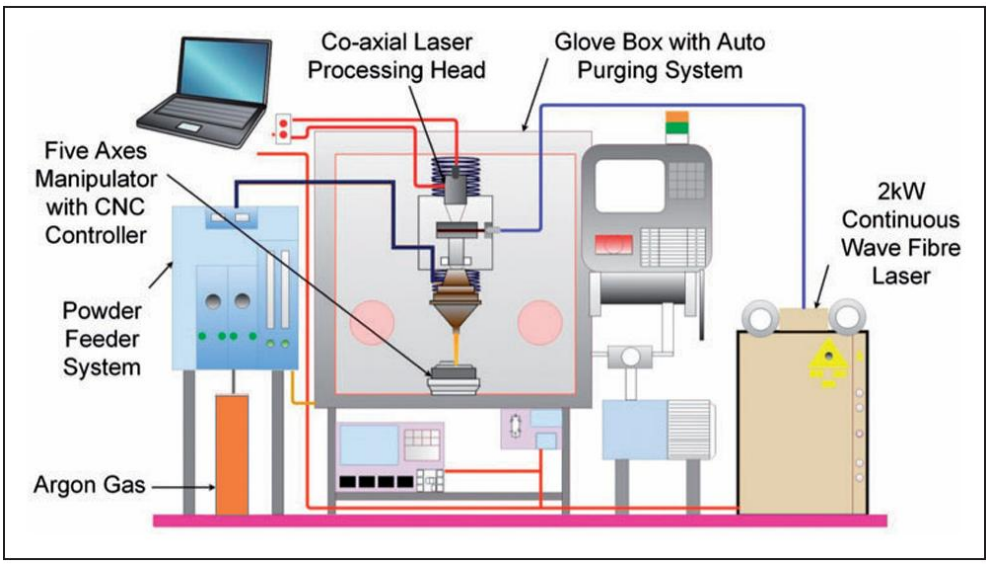

Fig. 3.2: Illustration of TVASHTR system [50].

Core Components of the Setup

A. Deposition Chamber and Motion Control:

The setup consists of a glove-box style chamber that is optionally vacuum-sealable and inert-gas purgeable. A three-axis gantry system forms the primary motion platform, with the base platform incorporating two rotational axes, thus offering five degrees of freedom for complex part fabrication. Motion is controlled via a Mitsubishi M80-A CNC controller, which ensures precise synchronization between toolpath and deposition parameters.

B. Laser System:

A 2-kW continuous-wave (CW) Ytterbium-doped fiber laser from IPG Photonics serves as the energy source. The laser operates at a wavelength of 1080 ± 5 nm, and is optically conditioned using a collimating unit (20 mm beam diameter) and a focusing lens of 200 mm focal length. The distance between the lens and the substrate is fixed at 215 mm, and the stand-off distance (SOD) from the nozzle tip to the workpiece is maintained at 11 mm.

C. Powder Feeding System:

A dual-hopper powder feeder delivers feedstock to the nozzle through pressurized argon gas. The system is configured for coaxial powder injection, with three equidistant feed inlets (separated by 120°) at the nozzle, ensuring uniform powder distribution around the laser beam. The powder feed angle into the melt pool is maintained at 18 degrees for optimal

interaction with the laser-induced melt pool. The feedstock used is Inconel 718 powder, with particle sizes ranging from 46 µm to 104 µm. The carrier gas flow rate for powder transport is maintained at 6 liters per minute (LPM).

D. Shielding and Carrier Gas System:

Argon gas is employed both as the central shielding gas and as the carrier gas for powder transport. The central shielding gas flow rate is maintained at 12 liters per minute (LPM) to provide an inert environment at the melt pool and to minimize oxidation during deposition.

E. Control Interface and Software Integration:

The laser power is independently controlled via a dedicated PC-based interface, allowing real-time adjustment of energy input. The motion system and powder feeders are controlled via the numerical controller (Mitsubishi M80-A). Mastercam is used for part design and toolpath generation, allowing direct import of CAD models and facilitating layer-wise build strategies.

Table 3.1: Fixed parameters of laser setup.

Parameter	Value
Laser Type	IPG Photonics Yb-doped fiber
Laser Power	2 kW (Continuous Wave)
Laser Wavelength	1080 ± 5 nm
Beam Diameter (Pre-focal)	20 mm
Focal Length	200 mm
Stand-Off Distance (SOD)	11 mm
Powder Feed Angle	18°
Powder Feed Configuration	3-way coaxial (120° separation)
Powder Particle Size	46–104 µm (Inconel 718)
Shielding & Carrier Gas	Argon
Central Gas Flow Rate	12 LPM
Carrier Gas Flow Rate	06 LPM
Control System	Mitsubishi M80-A CNC
Software Platform	Mastercam (CAD & Toolpath)

The process is performed under open ambient environmental conditions, i.e., without active thermal enclosure or atmospheric chambering, making it representative of industrial-scale operations. This configuration allows for studying the effects of process parameters under realistic fabrication scenarios and serves as a testbed for model validation and deposition strategy optimization.

3.2 Materials

For deposition of INCONEL718 (Osprey 718 powder from Sandvik) has been used with powder size in the range of 45-104 micrometre, & following chemical composition.

Table 3.2: Chemical composition of In718 by % [51].

Ni – Nickel	50 – 55 %
Fe – Iron	Bal.
C – Carbon	≤0.08 %
Cr – Chromium	17.0 – 21.0 %
Mo – Molybdenum	2.8 – 3.3 %
Nb – niobium	4.75 – 5.5 %
Mn – Manganese	≤ 0.35 %
Si – Silicon	≤ 0.35 %
P – Phosphorus	≤ 0.015 %
S – Sulfur	≤ 0.015 %
B – Boron	≤ 0.006 %
Cu – Copper	≤ 0.3 %
Al – Aluminum	0.2 - 0.8 %
Ti – Titanium	0.65 – 1.15 %
Co – Cobalt	≤ 1.00 %

3.3 Sample Preparation

All depositions are carried out on a 75 mm Dia and 15 mm thick circular substrates of SS304. To examine the microstructural characteristics, micro-indentation hardness and strength analysis, the samples were sectioned across

the cross-section using a wire electro-discharge machining (EDM) system (CONCORD Wire EDM, DK7732). The specimens were then processed following standard metallographic techniques to ensure accurate material characterisation. Special precautions were taken to minimize excessive heat generation, preventing potential damage to the samples. Sample preparation, adhering to established metallographic procedures, is crucial
for material characterisation. This process involves a sequence of steps to ensure precise material analysis. The observation surface underwent polishing using abrasive papers, ranging from coarse (~80) to fine (~2000), followed by diamond abrasive polishing to achieve a mirror-like finish and reduce imperfections. To contrast, Electro chemical etching was applied to polished sample using 10% Oxalic acid solution. These etching processes allowed for the Contrast visualization of deposited track. Optical analysis provided valuable insights into geometry of deposited track.

3.4 Optical Characterisation

A Metavis model advanced motorized metallurgy microscope was employed to measure track geometry and analyse surface topography of the built samples having capability of magnification of 5X to 50X. This instrument offers enhanced visualization capabilities, enabling precise measurements and detailed examination of surface features. The images are taken with 100 µm scale and then analysed using the open-source ImageJ Software.

Fig. 3.3: Optical Microscope Setup.

3.5 Strength analysis

The tensile strength of the deposited samples was analysed using ASTM standard tensile testing procedures with a Shimadzu AGX-V universal testing machine at a crosshead speed of 1 mm/min. Tensile specimens with a gauge length of 4 mm, width of 3 mm, and thickness of 1 mm were prepared for micro-tensile testing. Due to limited material availability and the small scale of the fabricated samples, the testing followed the methodology outlined in ASTM E345 Standard Test Method with necessary adaptations.

Fig. 3.4: UTM Setup for Tensile Test.

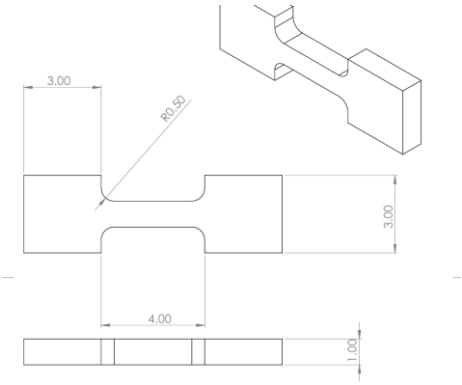

Fig. 3.5: Illustration of Micro Tensile Sample .

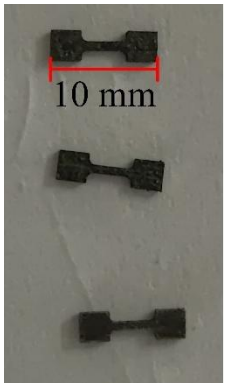

Fig. 3.6: Micro Tensile Samples.

Fig 3.7: Tensile Sample After Failure.

3.6 Hardness Test

Micro-indentation hardness testing was performed using Vickers hardness test to evaluate the hardness distribution along the build direction, where a square-based pyramidal diamond indenter with specified face angles is pressed into the

material under controlled conditions. After applying and removing the test force, the diagonal lengths of the indentation are measured to determine the Vickers hardness number (HV). This number is calculated as the applied test force F (kgf) divided by the surface area (AS) of the indentation (mm^2), as expressed by:

$$HV = \frac{F(kgf)}{AS(mm\text{^}2)}$$

The surface area (AS) is derived using the formula:

$$AS = \frac{d_{avg}^2}{1.8544}$$

Where d_{avg} represents the average diagonal length of the indentation.

$$d_{avg} = \frac{d1 + d2}{2}$$

Fig. 3.8: Vicker Hardness Test Setup.

For this study, a Mitutoyo HM-210 Type A or UHL VMHT Vickers hardness tester was used. A 300kgf load was applied for a total duration of 18 seconds, which included a loading time of 4 seconds, a hold time of 10 seconds, and an unloading time of 4 seconds. Hardness values were measured along a vertical line at the centre of the deposited beads or multilayer structure, and the average values were taken for comparative analysis.

Chapter 4

Observations, Results and Discussions

This chapter presents and interprets the outcomes of the experimental investigations performed on Laser Powder Directed Energy Deposition (Laser-DED) of Inconel 718, in accordance with the experiment design of this thesis. The experimental results include process trials, full factorial depositions, predictive modelling validation, and mechanical testing. Each observation is followed by analysis and discussion of trends, parameter influences, and comparison with existing literature, where appropriate. The aim is to build a comprehensive understanding of how laser power, scan speed, and powder feed rate influence bead geometry and quality, and how statistical and machine learning models can be leveraged to predict and optimize these outputs.

4.1 Preliminary Experiment and Parameter Influence

Initial experiments were conducted to understand and verify the sensitivity of geometric outputs to individual process parameters targeted in this thesis. An ANOVA analysis was performed to assess the significance of factors—laser power, scan speed, and powder feed rate—on bead width and height.

Table 4.1: ANOVA result for trial experiment.

	F-Value	P-Value	F-Value	P-Value
P1	11.69	0.000074	2.939	0.054579
P2	0.929	0. 480024	1.874	0.138015
P3	1.552	0. 228025	7.075	0.001547

The ANOVA results indicate that for track width (O1), laser power (P1) had the most statistically significant influence, with a p-value well below 0.05, confirming its effect at the 95% confidence level. In contrast, powder feed rate (P3) did not exhibit significant influence on track width. Although scan speed (P2) did not show statistically significant impact on either track height (O2) or

track width (O1) based on ANOVA, it is hypothesized that scan speed plays a more nuanced role, particularly in maintaining uniformity and stability of the melt pool rather than directly influencing geometry under conditions where deposition is already established.

For track height (O2), powder feed rate (P3) emerged as the most significant factor, with a p-value well below 0.05, indicating strong statistical relevance. Laser power (P1) showed a marginally significant effect on height, suggesting that height is influenced by both material availability and energy input, but more sensitively by the volume of material being delivered into the melt pool. These statistical insights are complemented by a correlation heatmap, which was generated to further explore interdependencies between process parameters and geometric outputs.

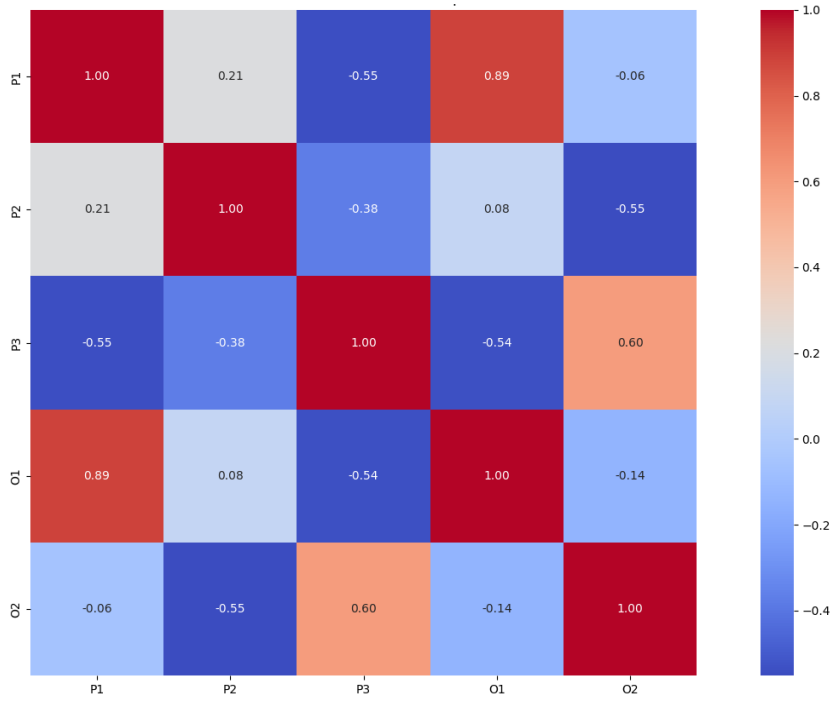

Fig. 4.1: Correlation heatmap.

The correlation heat map reveals a strong positive correlation between laser power (P1) and track width (O1) ($r \approx +0.85$), indicating that higher energy input significantly contributes to lateral melt pool expansion. Scan speed (P2) shows a moderately negative correlation with track height (O2) and a negligible correlation with width, supporting the hypothesis that scan speed primarily affects the uniformity and consistency of the deposition process rather than

directly influencing geometric dimensions. When deposition conditions are stable, scan speed appears to influence track width indirectly through its effect on height and layer continuity. Powder feed rate (P3) demonstrated a moderate positive correlation with track height and a moderate negative correlation with track width, suggesting that increased material input contributes to vertical build-up but may lead to narrower bead formation due to insufficient lateral melt pool spread. These correlations provided critical insight for defining parameter bounds in the subsequent full factorial experimental design.

A full factorial design with three input parameters at three levels each was employed to generate a complete dataset of bead geometries. The outputs—bead height, width, depth, and area—were recorded for each of the 27 combinations.

Table 4.2: Optical characterisation of full factorial depositions.

P1W	P2S	P3W	Height	Depth	Width	Image	Area
watts	mm/min	g/min	mm	mm	mm	590pixels/mm	mm^2
900	400	4.7	0.41	0.28	2.23		1.05
900	500	4.7	0.34	0.26	2.09		0.97
900	600	4.7	0.23	0.31	2		0.74
700	400	6.0	0.28	0.27	1.79	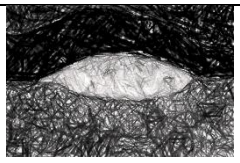	0.62
700	500	6.0	0.26	0.31	1.73		0.59

700	600	6.0	0.23	0.31	1.73		0.53
800	400	6.0	0.37	0.32	1.98		0.90
800	500	6.0	0.29	0.32	1.82		0.71
800	600	6.0	0.26	0.33	1.69	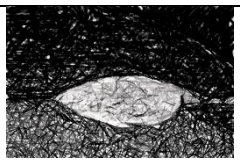	0.62
900	400	6.0	0.39	0.37	2.17	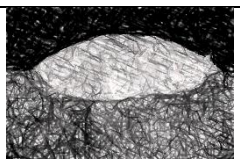	1.12
900	500	6.0	0.32	0.32	2.23		0.92
900	600	6.0	0.31	0.32	2.11	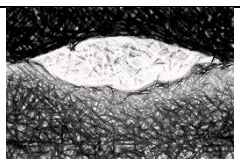	0.85
700	400	7.8	0.44	0.24	1.69	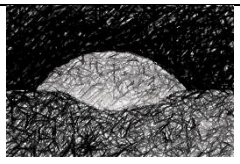	0.72
700	500	7.8	0.31	0.3	1.62		0.59
700	600	7.8	0.25	0.32	1.53	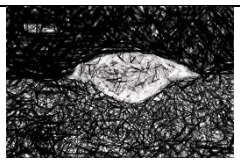	0.50

800	400	7.8	0.48	0.3	2.08		0.98
800	500	7.8	0.35	0.29	1.91	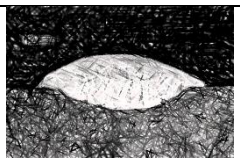	0.79
800	600	7.8	0.3	0.29	1.77	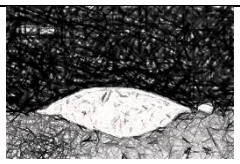	0.61
900	400	7.8	0.51	0.25	2.3	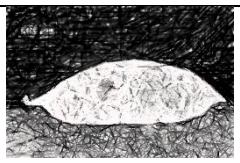	1.16
900	500	7.8	0.36	0.35	2.11	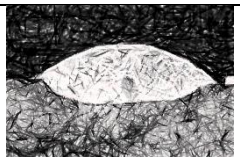	0.98
900	600	7.8	0.41	0.22	2.07	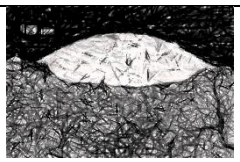	0.84
700	400	4.7	0.28	0.53	1.87	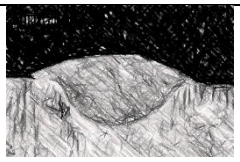	0.91
700	500	4.7	0.21	0.52	1.87	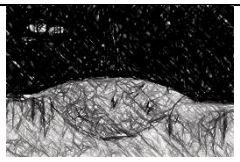	0.81
700	600	4.7	0.25	0.44	1.69	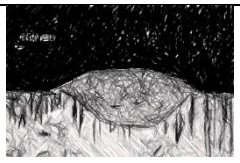	0.74
800	400	4.7	0.34	0.63	2.04	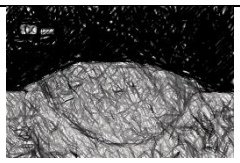	1.30

800	500	4.7	0.27	0.55	1.87	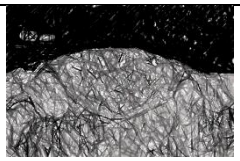	0.96
800	600	4.7	0.2	0.51	1.82	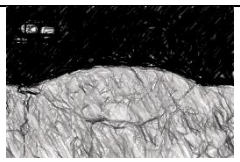	0.87

The results indicate clear trends. At constant scan speed, increasing laser power significantly increased bead height and width, while excessive power at lower scan speeds led to surface roughness and partial over-melting. Conversely, higher scan speeds led to narrower beads and insufficient fusion. The powder feed rate had a pronounced effect on bead height and dilution, particularly at lower power levels.

The aspect ratio (W/H) serves as a reliable indicator of melt pool morphology and is commonly used to identify the preferred working range in laser powder DED processes. In this study, all depositions from the full factorial experiment exhibited W/H values within the typical range of 3 to 6, which corresponds to the transition mode of operation. This mode is characterized by a stable melt pool, good bonding quality, and reduced risk of defects compared to keyhole or conduction modes, making it ideal for additive manufacturing applications.

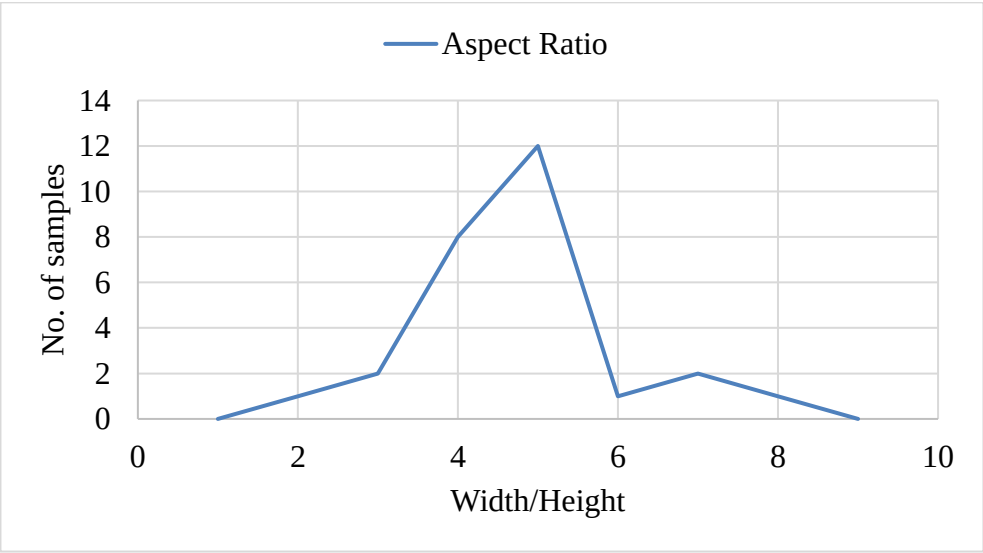

Fig. 4.2: Aspect Ratio Spread of all the deposited track.

4.2 Model Validation and Error Analysis

To evaluate the reliability and generalization capability of the developed predictive models, a set of test tracks were deposited using process parameter combinations not included in the training dataset. The geometry of these test tracks was measured and compared with model-predicted outputs for track height (O2), track width (O1), and track depth (O3).

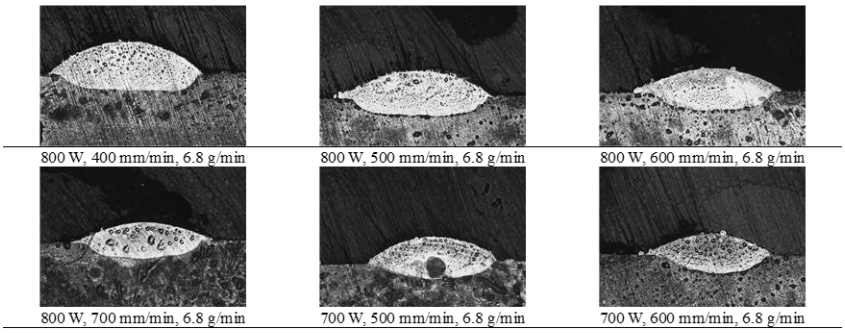

Fig. 4.3: Test track depositions.

Figure 4.3 shows the cross-sectional macrographs of six representative test tracks etched and imaged under optical microscopy. These sections reveal a range of bead morphologies and quality characteristics influenced by the chosen parameter combinations.

Among the six samples, some tracks show smooth bead boundaries with consistent dilution, while others exhibit notable porosity, undercuts, or uneven fusion at the base. These visual observations indicate that although the macro-geometry may be reasonably predicted, microstructural defects remain sensitive to local variations in powder–laser interaction and thermal gradients.

4.2.1 Height Prediction Analysis

Figure 4.4, illustrates the comparison between actual and predicted bead heights across the six test samples. The predicted values closely follow the actual measurements, with deviations remaining within acceptable limits for most samples. The average error in height prediction was below ±5%, suggesting strong agreement between model and experimental data.

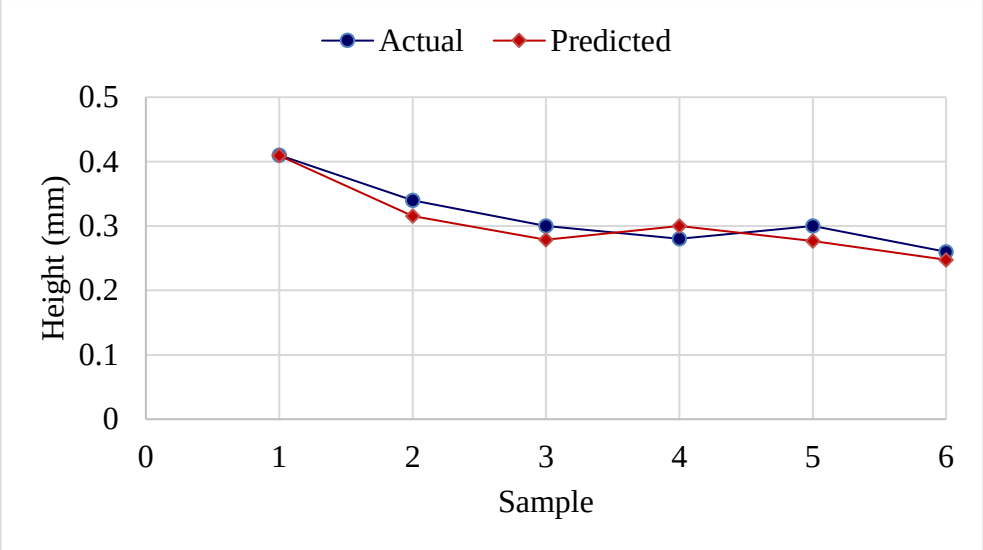

Fig. 4.4: Actual vs Predicted Height.

The high accuracy in height prediction is attributed to the direct influence of laser power and powder feed rate—both well captured during model training. These results validate the model's robustness for height prediction within the explored process window.

4.2.2 Depth Prediction Challenges

Figure 4.5 presents the parity plot for actual vs predicted track depth values. In contrast to height, depth prediction was less accurate, with visible and consistent overestimation by the model across all test cases. The predicted depth values cluster closely together, while the actual values show broader variance.

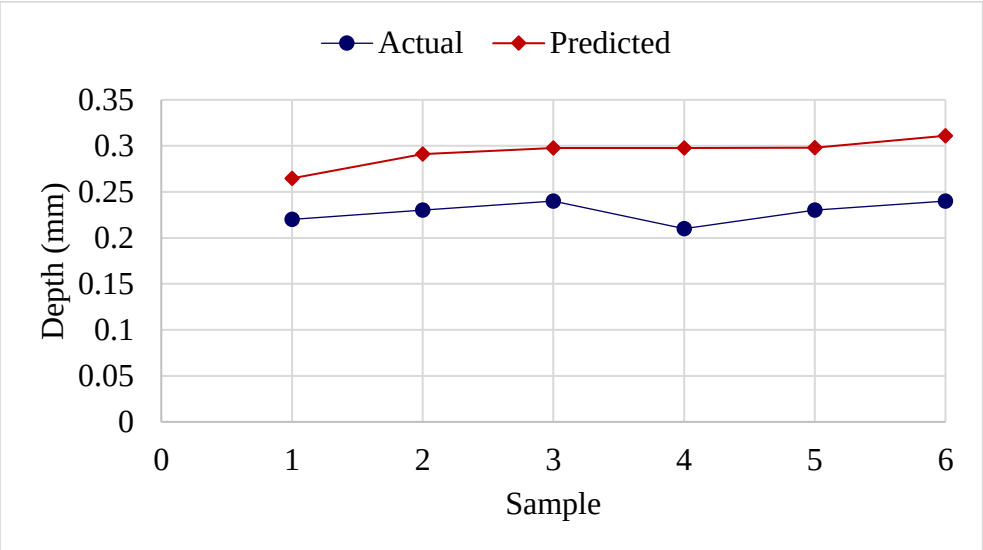

Fig. 4.5: Actual vs Predicted Depth.

The limited reliability of the depth model is likely due to challenges in accurately defining the true dilution zone during measurement. The overlap between the heat-affected zone (HAZ) and actual dilution boundary in etched cross-sections may have introduced ambiguity in depth quantification. This is a known issue in optical microscopy-based depth analysis, especially for materials like Inconel 718 where thermal gradients are steep and melt pool boundaries are diffuse. As a result, depth prediction was excluded from subsequent optimization studies, and future work may require enhanced imaging (e.g., SEM + EDS mapping) or thermal simulations to better quantify and model melt pool depth

4.2.3 Width Prediction Analysis

The comparison between the predicted and actual track width (O1) values for the test tracks is shown in Figure 4.6. Overall, the model demonstrated satisfactory performance in estimating bead width, with the predicted values closely tracking the actual measurements for most samples. The deviations were generally within a ±5–7% range, indicating that the width predictions were reasonably accurate, although slightly less precise than those for height.

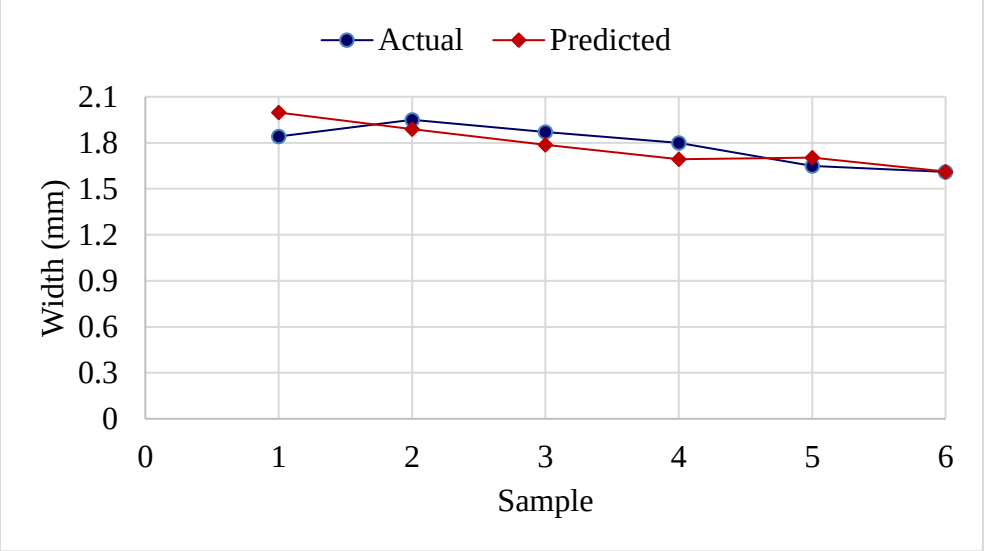

Fig. 4.6: Actual vs Predicted Width.

4.3 Hardness

To evaluate the effect of interlayer cooling time on the mechanical response of the deposited walls, microhardness measurements were carried out along the

build direction for three multilayer wall samples fabricated with different time delays (TD = 0 s, 4 s, and 8 s) between successive layers. Figure 4.7 illustrates the Vickers hardness ($HV_{0.3}$) values measured at incremental distances from the substrate up to 8 mm height.

The results reveal a clear trend in which hardness tends to decrease progressively from the substrate towards the top layers for all three samples. This gradient is particularly pronounced in the wall with TD = 8 seconds, which exhibits the lowest hardness values overall, with a final layer hardness dropping below 200 HV. In contrast, the wall fabricated with no delay (TD = 0 s) maintains the highest average hardness throughout the build height, remaining consistently above 230 HV.

This behavior can be attributed to the thermal history and cumulative heat input during layer-by-layer deposition. With no interlayer delay, heat from previous layers is retained, leading to thermal accumulation and a quasi-continuous solidification environment. This promotes rapid solidification and the formation of finer cellular dendritic structures, which are known to enhance microhardness in Inconel 718 due to higher dislocation density and solute trapping. Conversely, increasing the interlayer time delay allows each layer to cool more extensively before the next one is deposited, resulting in lower thermal gradients, coarser microstructures, and reduced hardness.

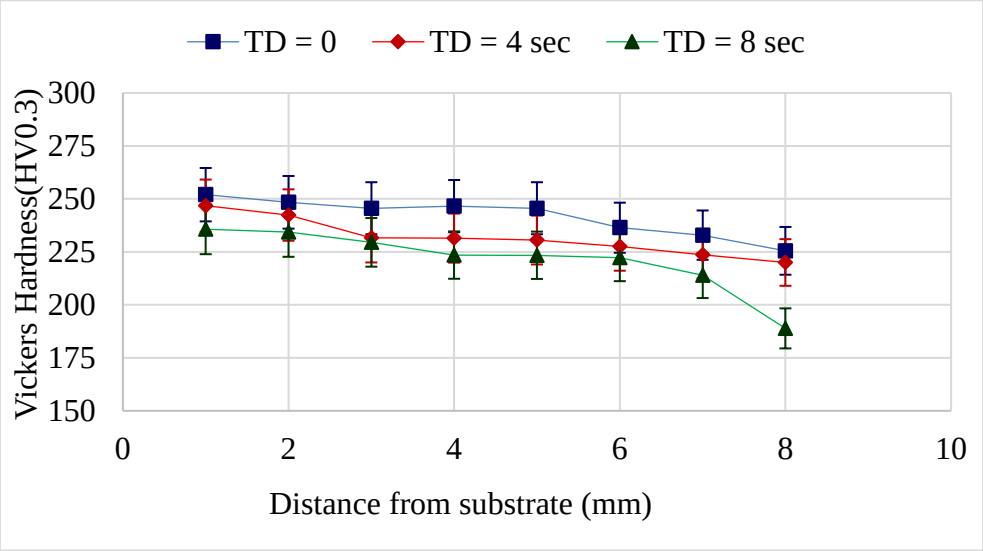

Fig 4.7: Micro indentation hardness tests data for thin wall depositions.

The decreasing hardness profile with build height also aligns with the understanding that the initial layers benefit from substrate conduction, while the upper layers are subject to reduced cooling efficiency and longer solidification times. This is further accentuated when additional delay is introduced, as seen with TD = 8 seconds.

These findings highlight the sensitivity of mechanical properties to thermal management strategies in laser-DED processes. They also emphasize the importance of process control during multi-layer deposition, particularly when targeting functionally graded structures or minimizing post-processing requirements.

4.4 Strength Analysis

To assess the mechanical integrity and anisotropy of the laser-deposited multilayer structures, tensile tests were performed on samples extracted along both the scan direction and build direction for three different interlayer time delays (TD = 0, 4, and 8 seconds). The results, summarized in Table 5.2, include ultimate tensile strength (UTS), strain at UTS, and strain at failure for each direction.

Table 4.3: Tensile test data.

Time Delay	Direction	UTS	% Strain at UTS	% Strain at Failure	Behaviour
0	Scan	810	31.9	35.75	Ductile
	Build	678.65	35.76	35.76	Ductile
4	Scan	1004	37.54	37.54	Ductile
	Build	661.8	32.67	37.54	Ductile
8	Scan	730.4	31.8	32	Ductile
	Build	626.8	27	32	Ductile

The tensile test results for the three multilayer IN718 walls fabricated with varying interlayer time delays (TD = 0 s, 4 s, and 8 s) reveal notable trends in strength and ductility. Among all samples, the TD = 4 s condition demonstrated the highest ultimate tensile strength (UTS) in the scan direction

(~1002 MPa), accompanied by considerable elongation (~37.5%), indicating a balanced combination of strength and ductility. The TD = 0 s sample exhibited moderately lower UTS (~810 MPa) but still retained significant elongation (~35.8%), suggesting that minimal dwell time leads to a slightly softer but ductile build.

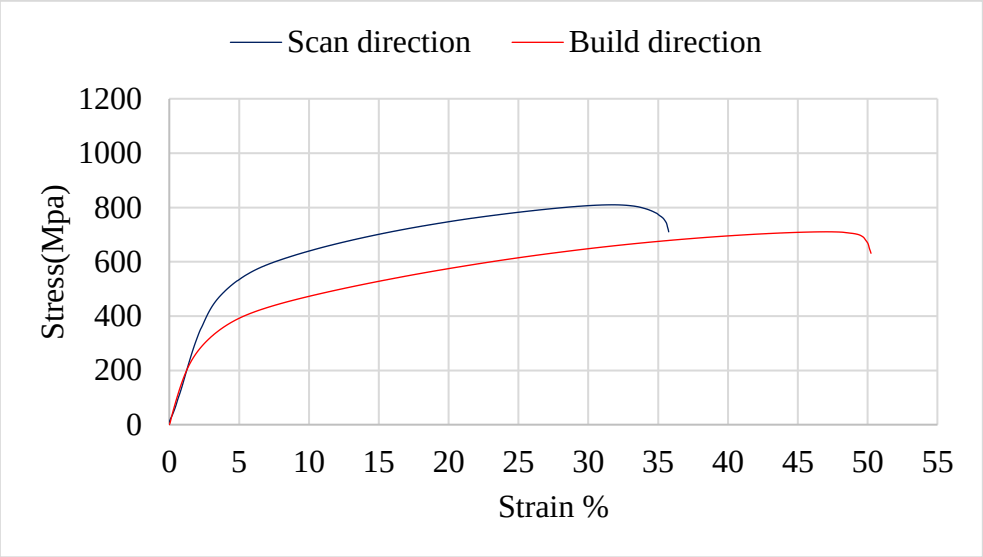

Fig. 4.8: Tensile Plot of TD = 0 sec Wall.

In contrast, the TD = 8 s sample showed reduced UTS (~730 MPa in scan direction), with a relatively lower strain at failure (~31.9%), indicating that prolonged interlayer cooling may have led to poor layer bonding or increased porosity, both of which could degrade tensile performance. Across all samples, the tensile behaviour in the build direction was consistently lower than in the scan direction, with UTS values dropping to ~626–678 MPa, reinforcing the known anisotropy in L-DED builds due to the columnar grain structure and interlayer interfaces.

Overall, the results emphasize the importance of thermal management during deposition. A controlled interlayer delay (around 4 seconds in this case) helps balance thermal gradients, improves fusion quality between layers, and ultimately enhances mechanical performance. These insights are consistent with microstructural trends observed in similar studies on laser-based DED of IN718.

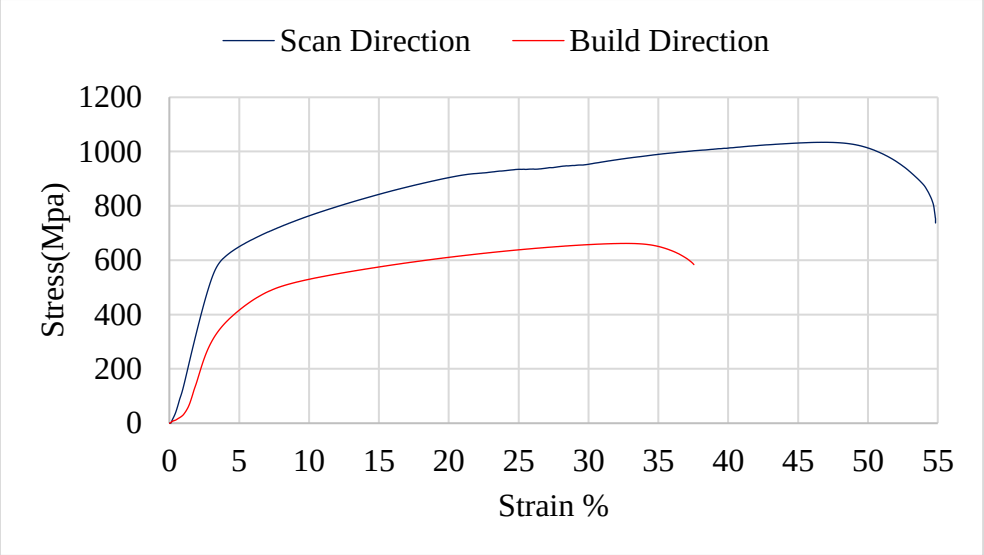

Fig. 4.9: Tensile Plot of TD = 4 sec Wall.

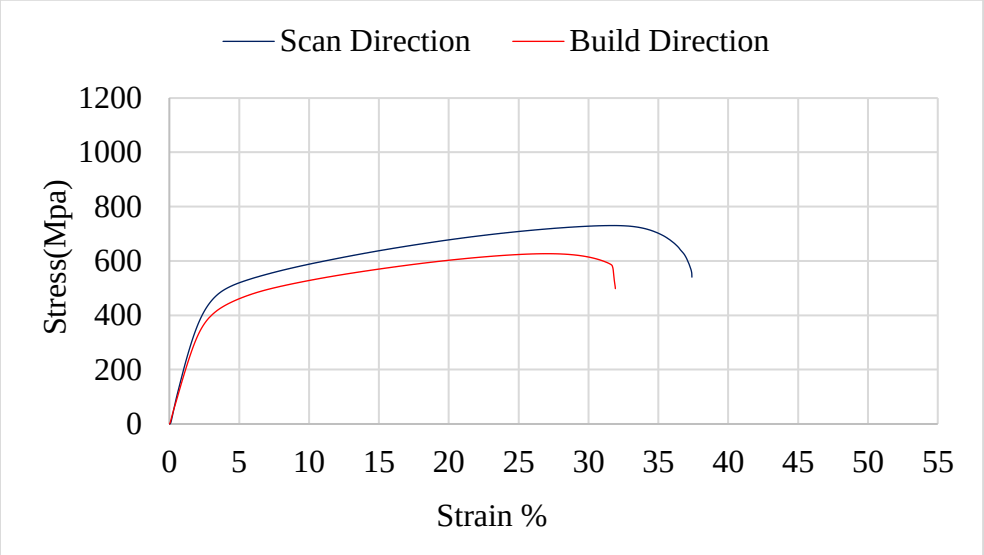

Fig. 4.10: Tensile Plot of TD = 8 sec Wall.

4.4.1 Anisotropy Between Scan and Build Directions

Across all time delays, samples tested along the build direction consistently recorded lower UTS values than their scan direction counterparts. For instance, at TD = 4 s, the build direction UTS was only 661.80 MPa, nearly 34% lower than the scan direction UTS. This anisotropic behaviour is typical in layer-by-layer AM processes and is largely attributed to:

- Layer interface quality
- Direction of heat flow and solidification

- Grain orientation, which tends to be columnar and aligned along the build axis

Moreover, strain at failure remained relatively comparable in both directions, confirming that while strength varied, ductility was retained regardless of orientation. This reflects the influence of thermal gradients and remelting behavior on the microstructure and bonding integrity between layers.

4.4.2 Overall Trends and Interpretation

These tensile test results reinforce the importance of thermal management during Laser-DED. Moderate interlayer delay (TD = 4 s) yielded the best mechanical performance by balancing heat retention for good interlayer bonding and allowing sufficient cooling to avoid thermal degradation. In contrast, both zero delay (TD = 0 s) and extended delay (TD = 8 s) compromised strength—either due to overheating or under-melting between layers.

The findings are consistent with microhardness trends observed earlier (Section 5.3), where the TD = 0 s wall had the highest average hardness due to finer microstructure but not the best tensile strength, likely due to internal residual stresses or non-uniform fusion. The TD = 4 s sample emerged as the most mechanically robust, confirming it as the most balanced strategy for multi-layer deposition under the given process conditions.

Chapter 5

Conclusions and Scope for Future Work

5.1 Conclusions

This research aimed to develop a robust, experimentally validated, data-driven framework for the prediction and optimization of geometric features in Laser Directed Energy Deposition (L-DED) of Inconel 718. By combining comprehensive experimental trials with machine learning and statistical modeling techniques, the study successfully achieved its objectives. The following key conclusions can be drawn:

A. Development of a Predictive Framework:

A hybrid predictive model was established using polynomial regression for track height and width prediction, and random forest for depth prediction. The model was trained on a full-factorial experimental dataset and demonstrated strong predictive accuracy for key geometric parameters.

B. Parameter Influence on Geometry:

Laser power and powder feed rate were found to be the most influential parameters on bead width and height, while scan speed exhibited more indirect effects related to melt pool stability. ANOVA and correlation analysis reinforced these trends.

C. Validation and Optimization:

Model validation using unseen test data showed excellent agreement for height (±5%) and width (±7%). Although depth prediction was less precise due to optical measurement challenges, the model still provided valuable trend-level accuracy. The model was then integrated into an optimization framework to reduce material usage, energy consumption, and build time.

D. Multi-Layer Build Demonstration:

The predictive framework was extended to multi-layer thin-wall deposition, incorporating interlayer control strategies. Experimental results showed that a 4-second interlayer delay yielded the highest

mechanical performance (UTS ≈ 1002 MPa) and maintained high ductility (~37.5%), confirming the positive influence of thermal control strategies.

E. **Mechanical and Microstructural Integrity:**
   Vickers microhardness profiling and tensile testing confirmed that interlayer thermal history directly influenced material hardness and strength. Reduced interlayer delay led to finer microstructures and higher hardness, but optimal mechanical properties were achieved with a balanced 4-second delay.

F. **Implication for DfAM**:
   The framework provides a valuable foundation for data-driven Design for Additive Manufacturing (DfAM), enabling accurate geometry prediction, process planning, and reduced reliance on post-processing in metal additive manufacturing workflows.

5.2 Scope for Future Work

While this study has laid a strong foundation, several opportunities exist to build upon and enhance the proposed framework:

A. **Integration with In-Situ Monitoring**:
   Incorporating real-time in-situ temperature monitoring—such as infrared thermography or pyrometry—can exponentially improve model fidelity. The observed enhancement in geometric quality and mechanical strength via controlled interlayer delay underscores the value of thermal feedback. Real-time data can enable closed-loop control, improving consistency and adaptability in L-DED processes.

B. **Enhanced Depth and Melt Pool Prediction:**
   Advanced imaging techniques like Scanning Electron Microscopy (SEM), Energy-Dispersive X-ray Spectroscopy (EDS), or thermal simulations can help improve the prediction of melt pool depth, which remains a challenge in this study due to the limitations of optical microscopy.

C. **Generalization to Complex Geometries:**

Future work should validate and extend the model's applicability to non-planar, multi-axis, and large-scale 3D components. This would confirm the model's scalability and reliability for real-world engineering parts.

D. **Machine Learning-Based Feedback Control**:

Leveraging the trained models within a real-time control loop, possibly enhanced by reinforcement learning or adaptive systems, can enable smart manufacturing systems that self-optimize during operation.

This study not only demonstrates the potential of data-driven methods in predicting and optimizing geometric features in L-DED of Inconel 718 but also provides a foundational framework that can be extended through real-time monitoring and intelligent process control to move towards a fully autonomous and adaptive additive manufacturing ecosystem.

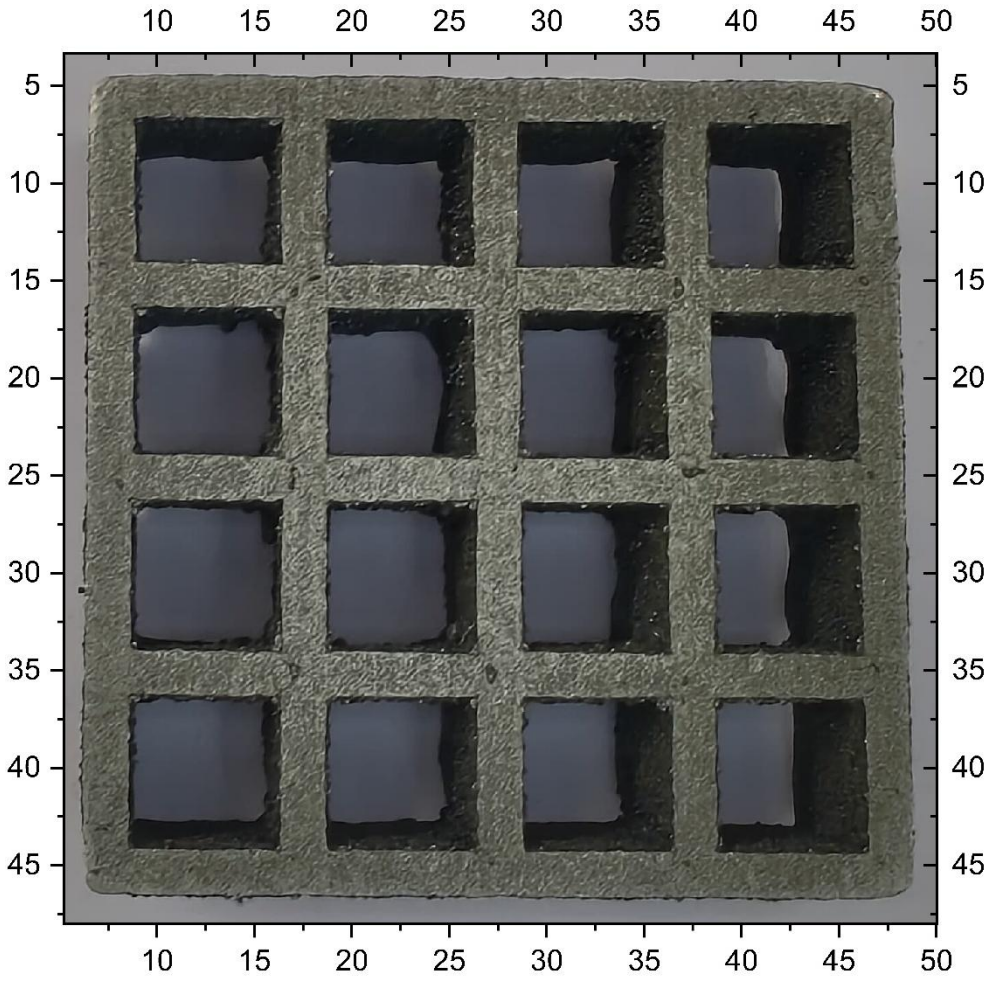

Fig 5.1: Final demonstration deposition (all dimensions in mm).

REFERENCES

[1] K. V. Wong and A. Hernandez, 'A Review of Additive Manufacturing', *ISRN Mechanical Engineering*, vol. 2012, pp. 1–10, Aug. 2012, doi: 10.5402/2012/208760.

[2] T. D. Ngo, A. Kashani, G. Imbalzano, K. T. Q. Nguyen, and D. Hui, 'Additive manufacturing (3D printing): A review of materials, methods, applications and challenges', Jun. 15, 2018, *Elsevier Ltd*. doi: 10.1016/j.compositesb.2018.02.012.

[3] B. Berman, '3-D printing: The new industrial revolution', *Bus Horiz*, vol. 55, no. 2, pp. 155–162, Mar. 2012, doi: 10.1016/j.bushor.2011.11.003.

[4] C. K. Chua and K. F. Leong, *3D Printing and Additive Manufacturing*. WORLD SCIENTIFIC, 2017. doi: 10.1142/10200.

[5] 'Wohlers Associates, "Vat photopolymerization Process Diagram,"'. Accessed: May 29, 2025. [Online]. Available: https://wohlersassociates.com/wp-content/uploads/2020/03/VPP_Ritter-768x514.jpg

[6] 'Wohlers Associates, "Material jetting Process Diagram,"'. Accessed: May 29, 2025. [Online]. Available: https://wohlersassociates.com/wp-content/uploads/2020/03/MJT_Ritter.jpg

[7] 'Wohlers Associates, "Binder jetting Process Diagram,"'. Accessed: May 29, 2025. [Online]. Available: https://wohlersassociates.com/wp-content/uploads/2020/03/BJT_Ritter.jpg

[8] 'Wohlers Associates, "Material Extrusion Process Diagram,"', Accessed: May 29, 2025. [Online]. Available: https://wohlersassociates.com/wp-content/uploads/2020/03/MEX_Ritter-1024x505.jpg

[9] 'Wohlers Associates, "Powder bed fusion Process Diagram,"', Accessed: May 29, 2025. [Online]. Available: https://wohlersassociates.com/wp-content/uploads/2020/03/PBF_Ritter-768x589.jpg

[10] 'Wohlers Associates, "Directed energy deposition Process Diagram,"'. Accessed: May 29, 2025. [Online]. Available: https://wohlersassociates.com/wp-content/uploads/2020/03/DED_Ritter-768x551.jpg

[11] 'Wohlers Associates, "Sheet lamination Process Diagram,"'. Accessed: May 29, 2025. [Online]. Available: https://wohlersassociates.com/wp-content/uploads/2020/03/SHL_Ritter.jpg

[12] C. P. Paul and A. N. Jinoop, 'Design for Additive Manufacturing', in *Additive Manufacturing*, 1st ed., vol. 1, New Delhi: Mc Graw Hill, 2021, ch. DfAM, pp. 123–150.

[13] I. Gibson, D. W. Rosen, and B. Stucker, *Additive Manufacturing Technologies*. Boston, MA: Springer US, 2010. doi: 10.1007/978-1-4419-1120-9.

[14] A. Gebhardt, 'Understanding Additive Manufacturing', in *Understanding Additive Manufacturing*, München: Carl Hanser Verlag GmbH & Co. KG, 2011, pp. I–IX. doi: 10.3139/9783446431621.fm.

[15] P. Parandoush and D. Lin, 'A review on additive manufacturing of polymer-fiber composites', Dec. 15, 2017, *Elsevier Ltd*. doi: 10.1016/j.compstruct.2017.08.088.

[16] T. DebRoy *et al.*, 'Additive manufacturing of metallic components – Process, structure and properties', Mar. 01, 2018, *Elsevier Ltd*. doi: 10.1016/j.pmatsci.2017.10.001.

[17] X. Wang, X. Gong, and K. Chou, 'Review on powder-bed laser additive manufacturing of Inconel 718 parts', Sep. 01, 2017, *SAGE Publications Ltd*. doi: 10.1177/0954405415619883.

[18] E. Hosseini and V. A. Popovich, 'A review of mechanical properties of additively manufactured Inconel 718', Dec. 01, 2019, *Elsevier B.V.* doi: 10.1016/j.addma.2019.100877.

[19] A. Kurdi *et al.*, 'Investigation into the Microstructure and Hardness of Additively Manufactured (3D-Printed) Inconel 718 Alloy', *Materials*, vol. 16, no. 6, Mar. 2023, doi: 10.3390/ma16062383.

[20] Z. Xu, C. Guo, Z. Yu, X. Li, X. Hu, and Q. Zhu, 'Microstructural evolution of inconel 718 alloy manufactured by selective laser melting under different stress conditions', in *MS and T 2019 - Materials Science and Technology 2019*, Materials Science and Technology, 2019, pp. 5–12. doi: 10.7449/2019/MST_2019_05_12.

[21] W. Keeley, R. Turner, B. Mitchell, and N. Warnken, 'A Development of the Rosenthal Equation for Predicting Thermal Profiles During Additive Manufacturing', *Thermo*, vol. 5, no. 2, p. 16, May 2025, doi: 10.3390/thermo5020016.

[22] P. Y. Lin, F. C. Shen, K. T. Wu, S. J. Hwang, and H. H. Lee, 'Process optimization for directed energy deposition of SS316L components', *International Journal of Advanced Manufacturing Technology*, vol. 111, no. 5–6, pp. 1387–1400, Nov. 2020, doi: 10.1007/s00170-020-06113-z.

[23] C. K. Yong, G. J. Gibbons, C. C. Wong, and G. West, 'A critical review of the material characteristics of additive manufactured in718 for high-temperature application', Dec. 01, 2020, *MDPI AG*. doi: 10.3390/met10121576.

[24] B. B. Ravichander, A. Rahimzadeh, B. Farhang, N. S. Moghaddam, A. Amerinatanzi, and M. Mehrpouya, 'A prediction model for additive

manufacturing of inconel 718 superalloy', *Applied Sciences (Switzerland)*, vol. 11, no. 17, Sep. 2021, doi: 10.3390/app11178010.

[25] D. Zhang, W. Niu, X. Cao, and Z. Liu, 'Effect of standard heat treatment on the microstructure and mechanical properties of selective laser melting manufactured Inconel 718 superalloy', *Materials Science and Engineering: A*, vol. 644, pp. 32–40, Sep. 2015, doi: 10.1016/j.msea.2015.06.021.

[26] P. Kumar, J. Farah, J. Akram, C. Teng, J. Ginn, and M. Misra, 'Influence of laser processing parameters on porosity in Inconel 718 during additive manufacturing', *International Journal of Advanced Manufacturing Technology*, vol. 103, no. 1–4, pp. 1497–1507, Jul. 2019, doi: 10.1007/s00170-019-03655-9.

[27] Y. Xv, Y. Sun, and Y. Zhang, 'Prediction Method for High-Speed Laser Cladding Coating Quality Based on Random Forest and AdaBoost Regression Analysis', *Materials*, vol. 17, no. 6, Mar. 2024, doi: 10.3390/ma17061266.

[28] A. K. Rai, C. P. Paul, G. K. Mishra, R. Singh, S. K. Rai, and K. S. Bindra, 'Study of microstructure and wear properties of laser borided Inconel 718', *J Mater Process Technol*, vol. 298, Dec. 2021, doi: 10.1016/j.jmatprotec.2021.117298.

[29] Y. Bian *et al.*, 'Statistical Analysis of Morphological Characteristics of Inconel 718 Formed by High Deposition Rate and High Laser Power Laser Cladding', *Materials*, vol. 17, no. 3, Feb. 2024, doi: 10.3390/ma17030638.

[30] T. Huynh *et al.*, 'Microstructural Development in Inconel 718 Nickel-Based Superalloy Additively Manufactured by Laser Powder Bed Fusion', *Metallography, Microstructure, and Analysis*, vol. 11, no. 1, pp. 88–107, Feb. 2022, doi: 10.1007/s13632-021-00811-0.

[31] S. Momeni, R. T. Coelho, J. G. Nuñez, and R. G. Jasinevicius, 'Effect of process parameters on the geometry of single-track deposits of Inconel 718 onto AISI4140 using laser cladding', *International Journal of Advanced Manufacturing Technology*, Oct. 2024, doi: 10.1007/s00170-024-14276-2.

[32] L. Fang, L. Cheng, J. A. Glerum, J. Bennett, J. Cao, and G. J. Wagner, 'Data driven analysis of thermal simulations, microstructure and mechanical properties of Inconel 718 thin walls deposited by metal additive manufacturing', Oct. 2021.

[33] Z. D. Zhang, S. Imani Shahabad, O. Ibhadode, C. F. Dibia, A. Bonakdar, and E. Toyserkani, '3-Dimensional heat transfer modeling for laser powder bed fusion additive manufacturing using parallel computing and adaptive mesh', *Opt Laser Technol*, vol. 158, Feb. 2023, doi: 10.1016/j.optlastec.2022.108839.

[34] Y. C. Shin, N. Bailey, C. Katinas, and W. Tan, 'Predictive modeling capabilities from incident powder and laser to mechanical properties for laser directed

energy deposition', *Comput Mech*, vol. 61, no. 5, pp. 617–636, May 2018, doi: 10.1007/s00466-018-1545-1.

[35] J. Wang, R. Zhu, Y. Liu, and L. Zhang, 'Understanding melt pool characteristics in laser powder bed fusion: An overview of single- and multi-track melt pools for process optimization', Oct. 01, 2023, *KeAi Communications Co.* doi: 10.1016/j.apmate.2023.100137.

[36] J. Li, Y. Yang, L. Chen, T. Yu, J. Zhao, and Z. Wang, 'Multi-Objective Optimization of Process Parameters in Laser DED Ni-Based Powder on Steel Rail Using Response Surface Design', *Coatings*, vol. 14, no. 4, Apr. 2024, doi: 10.3390/coatings14040401.

[37] B. L. Ribeiro *et al.*, 'Microstructural analysis of Inconel 718 manufactured via direct energy deposition: response surface methodology for process parameters optimisation and post-heat treatment', *Progress in Additive Manufacturing*, 2024, doi: 10.1007/s40964-024-00849-w.

[38] Y. Liu *et al.*, 'Optimization of parameters in laser powder deposition AlSi10Mg alloy using Taguchi method', *Opt Laser Technol*, vol. 111, pp. 470–480, Apr. 2019, doi: 10.1016/j.optlastec.2018.10.030.

[39] Y. Li *et al.*, 'Process parameter optimization of K477 and GH4169 for defect control in laser-directed energy deposition using Taguchi design of experiments', *International Journal of Advanced Manufacturing Technology*, vol. 131, no. 9–10, pp. 4447–4467, Apr. 2024, doi: 10.1007/s00170-024-13277-5.

[40] C. M. Knapp, T. J. Lienert, P. Burgardt, P. W. Hochanadel, and D. Kovar, 'A model to predict deposition parameters for directed energy deposition: part I theory and modeling', *Rapid Prototyp J*, vol. 25, no. 6, pp. 998–1006, Aug. 2019, doi: 10.1108/RPJ-08-2018-0221.

[41] M. Biyikli, T. Karagoz, M. Calli, T. Muslim, A. A. Ozalp, and A. Bayram, 'Single Track Geometry Prediction of Laser Metal Deposited 316L-Si Via Multi-Physics Modelling and Regression Analysis with Experimental Validation', *Metals and Materials International*, vol. 29, no. 3, pp. 807–820, Mar. 2023, doi: 10.1007/s12540-022-01243-3.

[42] A. N. Jinoop, C. P. Paul, S. K. Mishra, and K. S. Bindra, 'Laser Additive Manufacturing using directed energy deposition of Inconel-718 wall structures with tailored characteristics', *Vacuum*, vol. 166, pp. 270–278, Aug. 2019, doi: 10.1016/j.vacuum.2019.05.027.

[43] M. Yamaguchi, N. Kato, Y. Funada, T. Yachi, A. Saikai, and T. Furumoto, 'Influence of the laser power and powder feed rate on the porosity, dilution, and building efficiency of pure copper parts fabricated via directed energy

deposition with a blue laser', *International Journal of Advanced Manufacturing Technology*, Dec. 2024, doi: 10.1007/s00170-024-14789-w.

[44] D. J. Corbin, A. R. Nassar, E. W. Reutzel, A. M. Beese, and N. A. Kistler, 'Effect of directed energy deposition processing parameters on laser deposited Inconel® 718: External morphology', *J Laser Appl*, vol. 29, no. 2, May 2017, doi: 10.2351/1.4977476.

[45] B. Onuike and A. Bandyopadhyay, 'Additive manufacturing in repair: Influence of processing parameters on properties of Inconel 718', *Mater Lett*, vol. 252, pp. 256–259, Oct. 2019, doi: 10.1016/j.matlet.2019.05.114.

[46] N. Ghanadi *et al.*, 'Effect of LPBF Processing Parameters on Inconel 718 Lattice Structures: Geometrical Characteristics, Surface Morphology, and Mechanical Properties', *Mater Des*, vol. 253, May 2025, doi: 10.1016/j.matdes.2025.113864.

[47] W. Zhang, M. Tong, and N. M. Harrison, 'Scanning strategies effect on temperature, residual stress and deformation by multi-laser beam powder bed fusion manufacturing', *Addit Manuf*, vol. 36, Dec. 2020, doi: 10.1016/j.addma.2020.101507.

[48] V. Diwakar, A. Sharma, M. Z. K. Yusufzai, and M. Vashista, 'Analysis of the Thermal Residual Stress and Parametric Simulation in Laser Cladding Using COMSOL Multiphysics', *J Mater Eng Perform*, vol. 33, no. 15, pp. 7586–7595, Aug. 2024, doi: 10.1007/s11665-024-09390-x.

[49] M. Mueller, K. Franz, M. Riede, E. López, F. Brueckner, and C. Leyens, 'Influence of process parameter variation on the microstructure of thin walls made of Inconel 718 deposited via laser-based directed energy deposition with blown powder', *J Mater Sci*, vol. 58, no. 27, pp. 11310–11326, Jul. 2023, doi: 10.1007/s10853-023-08706-x.

[50] K. Benarji, Y. R. Kumar, C. Paul, A. Jinoop, and K. Bindra, 'Parametric investigation and characterization on SS316 built by laser-assisted directed energy deposition', *Proceedings of the Institution of Mechanical Engineers, Part L: Journal of Materials: Design and Applications*, vol. 234, no. 3, pp. 452–466, Mar. 2020, doi: 10.1177/1464420719894718.

[51] 'certificate-of-analysis-osprey-718-106-45'. Accessed: May 28, 2025. [Online]. Available: https://www.metalpowder.sandvik/en/webshop/metal-powders/superalloys/osprey-718/